

University Degree in Biomedical Engineering  
2022-2023

*Bachelor Thesis*

# “A compartmental model to investigate intracranial pulsatility”

---

Josué Pérez Sabater

Tutor

Wilfried Romain Stefan Coenen

Leganés, June 2023



**Attribution – Non-Commercial – No Derivatives**

© 2023. This work is licensed under [CC BY-NC-ND 4.0](https://creativecommons.org/licenses/by-nc-nd/4.0/).



## **ABSTRACT**

This project was motivated by the potential of mathematical models in the investigation and early detection of disorders related to the cerebrospinal fluid (CSF) system, such as syringomyelia and hydrocephalus. Abnormalities in the behavior of CSF pulsatility have been linked to various pathologies and computational models have emerged as a popular tool for simulating these intracranial fluid dynamics. By improving our fundamental knowledge on this subject, researchers aspire to detect these conditions at an early stage, enabling healthcare workers to address any potential obstruction, avoiding risky interventions and improving the quality of life of the patients.

The objective of this thesis is to develop a simple compartmental model that provides insightful indicators about CSF flow, intracranial pressure and other physiological properties. By integrating magnetic resonance imaging data from one individual, image processing in MATLAB and compartmental modeling, the dynamics of CSF flow were successfully simulated. The model used to produce the results was adapted to the characteristics of the subject and its predictions were compared with experimental data, to which it adjusted with accuracy. Additionally, some of the algorithms used in the processing of data proved their effectiveness at extracting flow signals from medical images. Automation of some tasks is suggested as a future research line, together with further validation of the developed model with clinical data.

### **Keywords**

Biomedical image processing, cerebrospinal fluid pulsatility, compartmental modeling, intracranial fluid dynamics, MATLAB.



## **ACKNOWLEDGEMENTS**

I would like to express my sincere gratitude to all those who have contributed to the completion of this bachelor's thesis. First and foremost, thank you to my thesis supervisor Prof. Wilfried Coenen for his guidance, expertise and support throughout this research project. I would also like to extend my appreciation to the faculty members of the Degree on Biomedical Engineering for the academic pathway they have shaped and the valuable knowledge they have imparted during my studies. Also, to the exceptional research body in the bioengineering laboratories at University Carlos III of Madrid. And last but not least, I would like to express my deepest gratitude to my family and friends for their unwavering support, understanding, and motivation throughout this academic journey.



# TABLE OF CONTENTS

<b>1. INTRODUCTION .....</b>	<b>1</b>
1.1. Biological background.....	1
1.2. Motivation .....	3
1.3. State of the art.....	4
1.3.1. Compartmental modeling .....	4
1.3.2. Computational fluid dynamics modeling .....	6
1.3.3. Alternatives to mathematical modeling.....	6
1.4. Objectives .....	7
1.4.1. Literature review.....	7
1.4.2. Flow acquisition from MRI .....	7
1.4.3. Model design and implementation .....	8
1.4.4. Model validation.....	8
<b>2. MATERIALS AND METHODS.....</b>	<b>9</b>
2.1. Model construction .....	9
2.1.1. Model workflow .....	9
2.1.2. Variables and simplifications .....	10
2.1.3. General equations .....	12
2.1.4. Specific equations.....	14
2.1.5. Equations with Fourier coefficients.....	18
2.1.6. Code implementation.....	19
2.2. Model study .....	21
2.2.1. Comparison of model variations .....	21
2.2.2. Tuning of matrix coefficients .....	22
2.2.3. Study of pathological conditions .....	24
2.3. Data acquisition and processing .....	24
2.3.1. Image acquisition.....	24
2.3.2. Metadata extraction .....	26
2.3.3. ROI selection .....	26
2.3.4. Aliasing removal .....	28

2.3.5.	Flow computation .....	30
2.3.6.	Results display .....	31
2.3.7.	Fourier coefficients .....	31
<b>3.</b>	<b>RESULTS AND DISCUSSION.....</b>	<b>33</b>
3.1.	Model outcomes .....	33
3.1.1.	Results of model comparison .....	33
3.1.2.	Results of coefficient tuning .....	34
3.2.	Data processing performance .....	36
3.2.1.	Results of aliasing removal .....	36
3.2.2.	Results of flow extraction .....	37
3.2.3.	Results of Fourier transformation .....	38
3.3.	Final review .....	39
3.3.1.	Results evaluation .....	39
3.3.2.	Limitations and future outlook .....	40
<b>4.</b>	<b>REGULATORY FRAMEWORK.....</b>	<b>42</b>
4.1.	Legislation analysis .....	42
4.2.	Technical standards .....	43
4.3.	Intellectual property .....	43
<b>5.</b>	<b>SOCIO-ECONOMIC ENVIRONMENT .....</b>	<b>44</b>
5.1.	Project budget .....	44
5.2.	Social impact .....	44
<b>6.</b>	<b>CONCLUSION .....</b>	<b>46</b>
	<b>BIBLIOGRAPHY.....</b>	<b>47</b>
	<b>ANNEX</b>	



## LIST OF FIGURES

Figure 1.1. Cerebrospinal fluid circulation pathways.....	1
Figure 1.2. Pathology of CSF-related disorders visualized in MRI .....	2
Figure 1.3. Research trend on CSF computational models .....	5
Figure 2.1. Model workflow and application .....	10
Figure 2.2. Diagrams depicting the general equations .....	13
Figure 2.3. Diagrams of the tested models .....	16
Figure 2.4. Detailed diagram of model C .....	22
Figure 2.5. Steps in the process of flow extraction .....	25
Figure 2.6. Regions of interest .....	27
Figure 2.7. Velocity mismatch due to encoding velocity constraints.....	28
Figure 3.1. Comparison of models .....	34
Figure 3.2. Tuning of venous compliance .....	35
Figure 3.3. Blood flow through each vessel along the cardiac cycle .....	37
Figure 3.4. Flow in and out of the cranial cavity.....	38
Figure 3.5. Comparison of original and reconstructed flow signals.....	39

## LIST OF TABLES

Table 2.1. Nomenclature of anatomical structures .....	15
Table 2.2. Order of variables in the system matrix .....	20
Table 2.3. Values used for constant parameters .....	23
Table 2.4. Example cases of aliasing removal.....	30
Table 5.1. Breakdown of the project budget .....	44

## **LIST OF ABBREVIATIONS**

<b>CC</b>	Cardiac cycle
<b>CFD</b>	Computational fluid dynamics
<b>CM</b>	Compartmental modeling
<b>CNS</b>	Central nervous system
<b>CSF</b>	Cerebrospinal fluid
<b>ECG</b>	Electrocardiogram
<b>MR or MRI</b>	Magnetic resonance (imaging)
<b>PTT</b>	Pulse transit time
<b>ROI</b>	Region of interest
<b>SAS</b>	Subarachnoid space
<b>UC3M</b>	University Carlos III of Madrid
<b>VENC</b>	Velocity encoding



# 1. INTRODUCTION

## 1.1. Biological background

The whole central nervous system (CNS), consisting of the brain and the spinal cord, is fully suspended in an aqueous substance called cerebrospinal fluid (CSF) within the dorsal cavity, enclosed by the cranium and the vertebral column. CSF is present in the spinal and cranial subarachnoid spaces (SAS) between the arachnoid and pia maters, but also within the ventricles and cisterns of the brain (see [FIGURE 1.1](#)). All these chambers are connected and allow the free flow of fluid across them [\[1\]](#). CSF is largely produced by ependymal cells in the choroid plexus of lateral ventricles. It flows into the third, then fourth ventricle and finally into the cisterna magna beneath the brain. From there, the fluid easily enters the SAS and part of it moves downward into the spinal sac. However, most of CSF will flow upwards around the cerebrum and it is believed to be reabsorbed by the arachnoid villi, which return it into the blood system through the venous sinuses in the cerebrum.

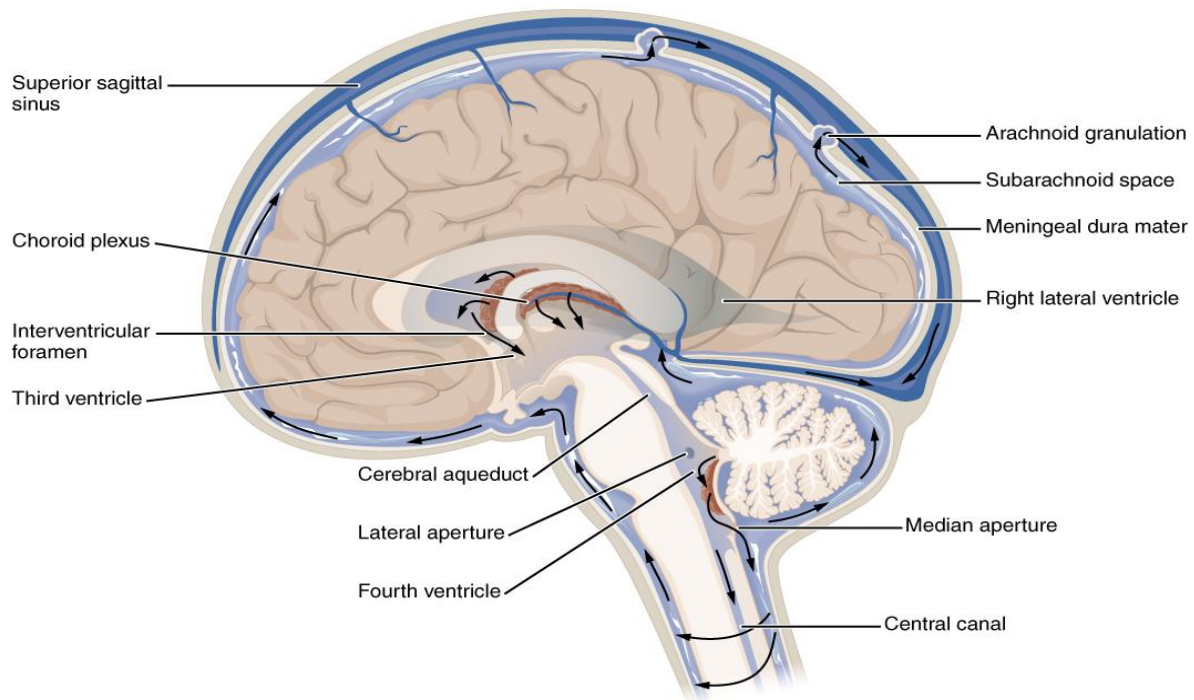


**Figure 1.1. Cerebrospinal fluid circulation pathways.** Sagittal section of the head. Black arrows indicate the direction of CSF flow starting at the choroid plexus (lateral and third ventricles) and ending in the arachnoid villi [\[2\]](#).

There are three main functions associated to the cerebrospinal fluid system: (1) nourishment of the brain with certain micronutrients that cannot cross the blood–brain barrier, but instead they diffuse through the choroid plexus into the CSF and then into the brain tissue [\[3\]](#); (2) clearance of waste products such as proteins, dead cells or other exogenous particles that leak out of the brain parenchyma through the recently discovered glymphatic system [\[4\]](#); and (3)

mechanical protection of the CNS from trauma by adding buoyancy to the brain, absorbing shocks and cushioning the brain against the skull. Additionally, arachnoid villi have the capacity of controlling pressure within the cranial cavity by adapting their absorption rate so that the pressure in the CSF-filled space remains the same or just above the pressure in the cerebral venous sinuses (around 10 mm Hg when lying horizontally) [1].

CSF presents two types of motion. Firstly, a bulk or directional motion arises because CSF is produced and reabsorbed at different places. Thus, a flow appears in the direction explained above: from the choroid plexus in the lateral ventricles towards the arachnoid villi in the cranial SAS. Secondly, there is a pulsatile or oscillation motion driven by the cardiac cycle (CC). Since the cranium is an enclosed, rigid cavity, intracranial pressure during systole rapidly increases as blood is injected through cranial arteries. To relief that pressure, some equivalent amount of CSF is displaced from cerebral to spinal SAS [5] crossing the foramen magnum. On the other hand, a reverse flow of CSF from the spinal cavity to the cranial vault is induced during diastole as blood is returned to the chest by the venous system. This constant oscillatory motion is known as CSF pulsatility.

There are certain conditions that can partially or totally block the arachnoid villi, affecting the reabsorption of CSF. Fibrosis, brain tumor and excess blood cells caused by hemorrhage or infection are examples of these conditions. When CSF is not adequately reabsorbed, pressure inside the cranial vault can be abnormally high, leading to changes in the pulsatile flow of CSF. Other diseases that disrupt the normal CSF flow include spinal cord tumor, spinal cord injury and Chiari malformation. All of these can cause a set of disorders such as papilledema, cerebral edema, hydrocephalus, syringomyelia and idiopathic intracranial hypertension. A correct pressure and flow within the CSF system are therefore fundamental to avoid complications.

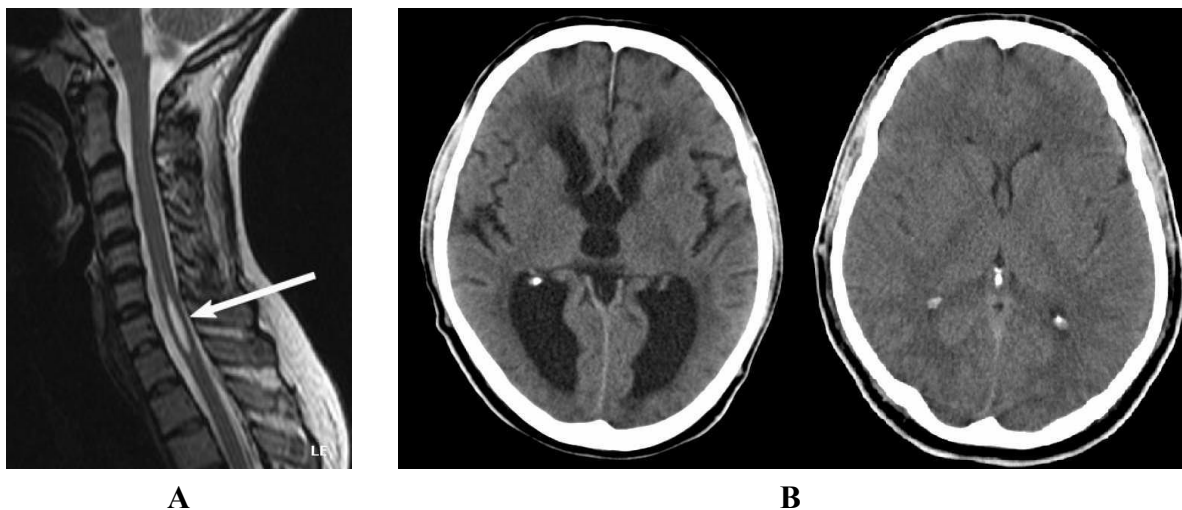


**Figure 1.2. Pathology of CSF-related disorders visualized in MRI.** (A) Sagittal section of the spinal cord of a patient with syringomyelia, with the white arrow pointing to the syrinx [6]. (B) Axial section of the brain of a patient with hydrocephalus (left) and a healthy individual (right); the enlargement of the ventricles in the hydrocephalic patient can be noticed [7].

Hydrocephalus is caused by an excessive accumulation of CSF in the ventricular cavities within the brain, which exerts high pressure on the surrounding tissues causing brain damage. Treatment involves creating a shunt to drain CSF from the ventricles and relieve pressure [8]. Syringomyelia, on the other hand, is characterized by the formation of a fluid-filled cyst (syrinx) in the central canal, which can enlarge, compress the spinal cord and damage the nerves. It is treated by draining the syrinx or by addressing the cause of the abnormal pressure in an attempt to restore normal CSF flow [9]. Both conditions can be observed in the magnetic resonance imaging (MRI or MR) slices of [FIGURE 1.2](#).

## 1.2. Motivation

The combined prevalence of hydrocephalus, syringomyelia and idiopathic intracranial hypertension is estimated to be of 169 people out of 100,000 [10] [11] [12] and, while these neurological disorders are not especially common among the population, their consequences without treatment are often life threatening. However, treatment for the first two conditions, hydrocephalus and syringomyelia, usually involves delicate surgeries and often are not definitive solutions: the patient needs to be monitored throughout their entire life and additional surgeries may be required. As a result of this and many other complications derived from the disorders, life quality of the patients is frequently diminished.

Given the severe consequences of CSF-related disorders, a better strategy to deal with these neurological conditions is to focus on early detection and intervention, sometimes even before symptoms appear. A premature diagnosis enables the healthcare workers to provide the patient with recommendations of a lifestyle that minimizes the risk of syrinx formation or ventricle enlargement. Furthermore, it offers the potential to address —by surgery— any obstruction that may become the source of syringomyelia, hydrocephalus and other similar pathologies, and it facilitates close monitoring of the disease evolution. With such objectives in mind, there is a growing interest in studying the dynamics of CSF pulsatility to gain deeper insights into the underlying mechanisms behind disorders caused by abnormal CSF flow. In fact, some studies have already linked different pathologies to flow parameters, such as increased mean peak systolic CSF flow in idiopathic syringomyelia [13] and an elevated pulsatility of the aqueduct CSF flow in idiopathic normal pressure hydrocephalus [14]. While these indicators are still being investigated and validated, they offer valuable information on the factors that may lead to disease.

Among the various methodologies available to obtain these indicators, mathematical modeling has been widely used to reproduce the internal anatomical structures and mechanics. Specifically, computational fluid dynamics models (CFD) have emerged as a popular approach for simulating intracranial fluid dynamics. These models have proved their efficacy in replicating the intricate 3D geometry of intracranial structures and simulating patient-specific CSF dynamics with high temporal and spatial accuracy [15]. However, the amount of computational resources needed to achieve such accuracy makes the

implementation of these models very expensive. A much more efficient alternative to CFD is compartmental modeling (CM), which does not consider the detailed shape of the compartments involved but rather defines them as conceptual spaces connected to each other [16]. CM proposes a simpler but still effective approach to replicate the alterations in blood and CSF flow throughout the CC, as well as the changes in pressure and volume of the different anatomical cavities within the skull. Data from MRI can be used as input to the model, which then reproduces the dynamics of the entire intracranial system, enabling the extraction of parameters related to CSF pulsatility. Consequently, the integration of CM with the predictive capability of these indicators holds promise for the detection and potentially the prediction of CSF-related disorders, and they could eventually play an important role in their diagnosis.

The compartmental model developed in this thesis will be part of a personal line of research by Professor Wilfried Coenen of University Carlos III of Madrid (UC3M), who proposed and supervised this project. The model will be used as a tool to obtain fundamental knowledge regarding the relationship between CSF dynamics and intracranial pressure. Eventually, this research aspires to aid in the creation of medical tools to support the early diagnosis of syringomyelia, hydrocephalus and other similar neurologic disorders that are caused or affected by an abnormal CSF flow and intracranial pressure. The focus during the design of the model will be set on simplicity and computational efficiency.

### **1.3. State of the art**

Mathematical models allow to predict the behavior of a system starting from a set of initial conditions or input. As [FIGURE 1.3](#) depicts, this type of model applied to the study of CSF pulsatility is becoming increasingly popular because it facilitates the investigation of fluid dynamics inside the skull and the mechanisms behind CSF disorders. Through the implementation of CM and CFD simulations, researchers have been able to advance our knowledge on CSF and blood fluid dynamics within the cranial and spinal cavities, to the point of linking some pulsatility parameters to the development or presence of pathologies. These achievements were possible with the use of a wide range of computational models with different characteristics and approaches, which are presented in this section.

#### **1.3.1. Compartmental modeling**

Compartmental models take a holistic approach to address the interconnected structures within the skull, representing cavities as conceptual spaces and studying flow, pressure and volume variations in each compartment as a whole, rather than at many spatial points. This methodology requires much less computational power than finite element modeling, which will be explained in the following section. They also neglect the geometric intricacies of intracranial anatomy, removing the need for high-resolution imaging techniques to map these



structures. Therefore, they are presented as a simple and cost-efficient alternative to the more complex CFD models.

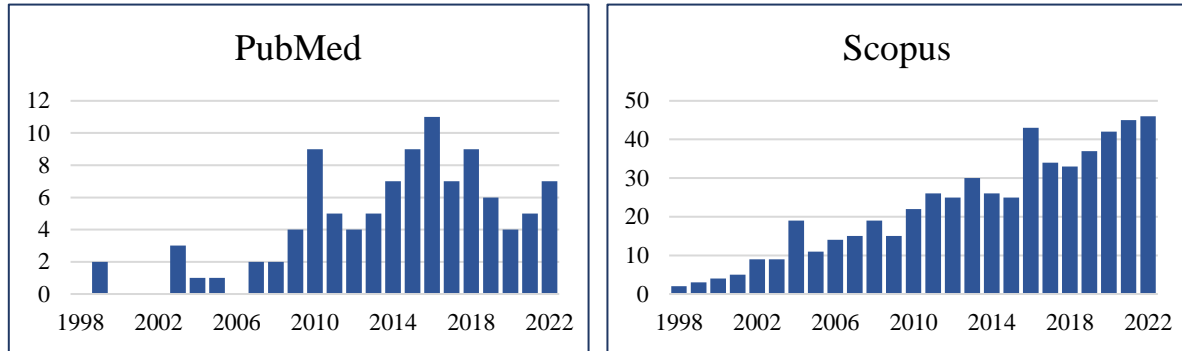


**Figure 1.3. Research trend on CSF computational models.** The two graphs display the number of scientific articles per year (from 1998 to 2022) retrieved using the following query: *(CSF) AND ((computational model) OR (computational fluid dynamics))*. Data retrieved from PubMed [17] and Scopus [18] databases.

One of the very first examples of a compartmental strategy to study intracranial pressure was offered by anatomist Alexander Monro [19] in 1783, who reflected on the necessity of a constant fluid volume within the cranium due to the rigidity of this one. This hypothesis was shared by his student George Kellie and has nowadays evolved into the well-established Monro–Kellie doctrine, which states that the total volume of brain, blood and CSF within the cranial cavity must stay constant at all times, and that an increase in one of them must be compensated by a decrease in the other two. Several studies have further elaborated on this idea by the development of CM that included more or less compartments, depending on the subject of study and intentions of the authors.

Sorek *et al.* [20] presented a seven-compartment model where the behavior of each compartment could be entirely described by the pressure inside and the exchange of fluid with contiguous compartments. Brain, blood and CSF in the model were governed by balance equations that depended on lumped resistance and compliance parameters, modeled as localized elements in the walls of the compartments. Nevertheless, the configuration used by Sorek *et al.* considered CSF to fill a unique, intracranial cavity and it lacked any connection to the spinal cord, which is known to be an extension of the subarachnoid space outside of the cranium. The spinal SAS plays a pivotal role in CSF dynamics because it constitutes an exit way for this fluid during systole, when blood enters the head and intracranial pressure increases. Consequently, posterior models have incorporated the spinal cavity as a separate compartment or extension of the cranial SAS. Different control volumes for CSF fluid are proposed by Cohen *et al.* [21], which range from defining specific ventricular cavities to including the totality of the CSF system in a single compartment. Linninger *et al.* [22] described the interaction between fluid and elastic tissue to compute ventricle deformations, which were used to derive CSF pulsatility and intracranial pressure at different brain ventricles from arterial pulsations at the choroid plexus. Another paper published by the same

author included a compliant spinal cavity and biphasic brain parenchyma, and the model was used to compare the results between healthy and hydrocephalic patients [23].

### **1.3.2. Computational fluid dynamics modeling**

While some examples of CM have been offered above, the increasing power and efficiency of computers have enabled researchers to implement more complex and demanding simulations. Advances in medical imaging, especially MRI, have made it possible to measure and recreate the three-dimensional anatomy of the interior of the skull, obtaining a digital copy of the different cranial cavities and tissues [24]. CFD models take advantage of these patient-specific 3D reconstructions to provide a high-resolution simulation of the CSF dynamics with great spatial and temporal accuracy. Once the geometry of the internal structures has been defined, a 3D mesh is used to divide the model into discrete, finite voxels where pressure and flow conditions are tracked and analyzed individually—a technique known as finite element method. Differential equations describing the balance of mass and momentum are defined and solved at each of these voxels. Together these data constitute an accurate representation of the totality of the system.

Although a growing number of research studies are implementing CFD to the subject at hand, their diversity and extension will not be fully covered in this report because the model developed for this project belongs to the compartmental category. However, the work presented by Causemann *et al.* in a recently published study [24] will be provided as a reference of the current state of the art in CFD modeling. This research team has developed a “coupled fluid-structure interaction model” where the effects of brain tissue motion, blood and CSF pulsatility and interstitial fluid exchange are all combined into a single system. Brain parenchyma and CSF-filled cavities were modeled as 3D spaces segmented from MRI data, bounded by the skull and discretized using a computational mesh. Porosity, permeability and elasticity of brain tissue were accounted for, stresses and strains were defined with tensors and the Navier–Stokes equations were used to describe velocity and pressure at each of the more-than-4.5 million mesh cells. Measures of interest were identified to obtain insights from the vast amount of data produced in the simulation.

From this methodology introduction, it can be seen that CFD models encompass a far more complex model design with an immense amount of data and parameters involved, which translates into an enormous increase in computational requirements. Besides, highly accurate imaging data is needed to validate the results of the simulation due to the high spatial resolution of the models. These are some of the reasons why the work presented in this thesis will focus on the development of a CM, where the predictions and calculations can be easily handled by any computer.

### **1.3.3. Alternatives to mathematical modeling**

Although computational modeling offers a powerful tool for simulating complex CSF flow dynamics in a non-invasive and accurate manner, there are some limitations to this

technology: assumptions on the geometry and material properties are often taken in order to simplify the computations so results may not fully represent the real, in vivo behavior; assessing the model performance requires access to high-quality medical imaging data, which is bound to limited availability and resources; generalized models do not respond accurately to patient variability, while patient-specific models are limited to the characteristics of a single individual and may not adapt well to a broader population; and finally, high-resolution CFD models are computationally demanding and entail the use of powerful computers.

Some alternatives include non-invasive imaging techniques, such as phase-contrast MRI and transcranial Doppler ultrasound [25], which are often used to obtain insights into CSF pulsatility instead of computational modeling. These methods are subject to specific technical equipment and requirements that may impose restrictions on their use. Additionally, some invasive methods can be used to obtain direct measurements of CSF pressure (lumbar puncture [26]) or intracranial pressure (intracranial pressure monitoring [27]), but they do not provide details about CSF flow or pulsatility and are not useful to understand its dynamics. On top of that, the invasiveness of the procedures may cause infections, complications and discomfort for the patient.

## **1.4. Objectives**

The purpose of this thesis is to help in the understanding of CSF pulsatility through the development of a mathematical compartmental model capable of simulating intracranial dynamics. In order to fulfill this purpose, specific objectives are defined.

### **1.4.1. Literature review**

Initial review of scientific articles, textbooks and other sources will be conducted in order to acquire essential background knowledge about intracranial physiology and dynamics, CSF pulsatility and related disorders, and state-of-the-art models similar to the one proposed.

### **1.4.2. Flow acquisition from MRI**

Input to the proposed model may be in the form of flow, pressure or volume. To create and test the model, flow information of real subjects extracted from MR images will be used. Processing these images will be a required task, which may be divided in the following steps:

- Segmentation of regions of interest: MR images contain information from a whole slice of the human body so segmentation of the vessels to be studied is required.
- Removal of velocity aliasing: cine-MRI produces a distorting aliasing artifact in the images which shall be corrected to obtain the desired results.
- Computation of flow: data provided by MRI needs to be transformed into useful, quantifiable flow signals for their use in the model.

- Transformation into Fourier coefficients: signals involved in the model would be represented as a set of complex Fourier coefficients, which introduces several advantages, as suggested by the supervisor of the thesis.

The objective of obtaining flow signals from real MRI data may be achieved by developing a MATLAB script capable of implementing the whole process, starting with the reading of MRI DICOM files, followed by solving the different tasks mentioned and finishing with the production of insightful charts displaying the evolution of flow over time.

#### **1.4.3. Model design and implementation**

Representing the main goal of the thesis, the creation of a simple and cost-effective compartmental model will be possible by means of a system of mathematical equations based on the real dynamics of CSF and blood within the head. Using part of the real flow signals obtained by MRI as input to the system, parameters of these equations will be tuned to make the output adapt to the remaining part of MRI-derived data, effectively adapting the model to the individual's characteristics. Inspiration from current models' workflow and methods may be useful.

#### **1.4.4. Model validation**

Once the model is complete, it shall be tested on new subjects and ideally on patients subject to the diseases mentioned earlier in the [MOTIVATION](#). Significant parameters derived from the model will be used as indicators to diagnose the existence of abnormalities in CSF pulsatility and intracranial pressure. These indicators can be defined with the help of already-published material and should be related to the presence or potential development of syringomyelia, hydrocephalus and other similar conditions.

## 2. MATERIALS AND METHODS

The model was conceived as a compartmental system of interdependent flows, pressures and volumes emulating the real dynamic behavior of the intracranial fluids and cavities. The system was designed with simplicity on the focus, taking assumptions to make the computations more efficient. An initial processing of patient images was necessary to extract blood and CSF flow information. These data would then be used together with fluid dynamics equations as the input to test the model. In this section, the methodology to build and test the model is explained in the first place, since this part addresses the main objective of the thesis. Next, a detailed explanation of the previous image processing is provided.

### 2.1. Model construction

This section will cover everything about the proposed model, from the physics and mathematical background to its application on intracranial structures and the implementation as a MATLAB script. Code fragments, equations and visual diagrams are provided to facilitate the understanding of the model.

#### 2.1.1. Model workflow

The goal of the model is to obtain insightful information about CSF pulsatility from some input experimental patient data, which may come in the form of changes in pressure or flow along the CC. The approach followed in this thesis to fulfill such objective was to gather fluid dynamics equations relating all relevant variables into a single mathematical system, so that introducing some input signal (for example, the evolution of carotid arterial flow during one CC) would result in the calculation of all other signals (flow, pressure and volume changes in blood, CSF and related cavities). Once the results have been obtained, further analysis may detect abnormal flow behavior or physiological conditions and help diagnose the potential presence or development of pathologies.

#### INPUT

A system of independent linear equations has one unique solution if all equations are consistent and the number of equations is the same as the number of unknowns. In our model, independently of the level of simplification, there was always one unknown more, leaving one empty row that could be used to introduce experimental data (and therefore fulfill the requirements for a unique solution). This additional input could be either the measured blood or CSF flow from MRI, as the diagram in [FIGURE 2.1](#) suggests, or any other variable of the system that the user may be interested in studying, such as the carotid pressure. As it will be explained, the input signal needs to be expressed as complex Fourier coefficients. If that is not the case, an additional step is taken to transform it into the desired form.

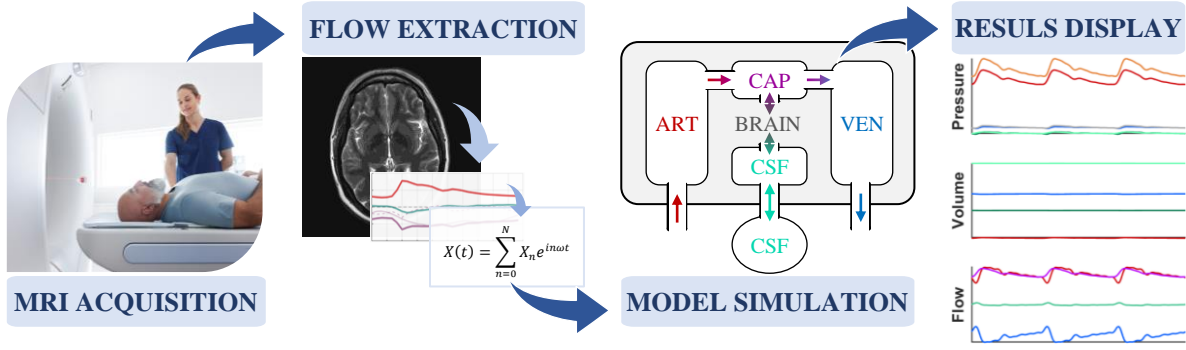


**Figure 2.1. Model workflow and application.** The different steps that need to be followed in order to implement the model are pictured. As an example, the input to the model is a flow signal, which needs to be interpreted from the MR images and transformed into Fourier coefficients before being delivered to the model. Output charts offer the simulation of pressure, volume and flow at different anatomical places. Images are original, except for the MRI scanner (stock image retrieved from Microsoft 365 creative content library) and MR brain image [28].

## OUTPUT

Upon formulating the fluid dynamics equations and establishing the input data, the model is ready to evaluate the system and predict the behavior of the remaining variables. This computation yields a set of Fourier coefficients for each signal that can be used to reconstruct them in the time domain. Pressure and volume of each intracranial cavity are simulated throughout the CC, along with the flows between compartments. All signals are graphically represented in time, facilitating their visual analysis and interpretation.

## APPLICATION

Finally, an additional step to bring the model closer to its practical application consists in the obtention of informative features that are somehow linked to known CSF disorders. Research on this topic [29] has already proved the relationship between some fluid dynamics parameters and different neurological pathologies. By taking velocity or pressure measurements of blood or CSF at a specific location, the pulsatile behavior can be extrapolated to other parts of the head and a range of useful attributes could be obtained and analyzed. A second approach to take advantage of the model is to use several measurements of the same patient to adjust the coefficients of the equations and find an estimation of subject-specific resistance and compliance values. This technique could be used to define the physiological properties of the patient's internal structures, potentially finding indicators of pathologies. The aspiration of this thesis is to validate the proposed model using real patient data and assess its effectiveness in correctly identifying the aforementioned conditions.

### 2.1.2. Variables and simplifications

There are three physical quantities involved in the mechanics of the model: pressure, flow and volume. These fundamental magnitudes are related to each other through mathematical equations, which will be discussed later in this section. A brief explanation of each variable

in the context of cranial fluid dynamics is provided next, together with the assumptions taken to simplify the system.

## PRESSURE

The driving force of blood dynamics and circulation is the heart. After cardiac contraction, the power exerted by the heart forces blood to flow into the cranial cavity, travel through cranial arteries, capillaries and veins to finally exit the head via the jugular veins. This event is represented in the model with a pressure difference between the entrance to arteries and the exit of veins. The pressure at the entrance of the first compartment,  $p_{car}$ , corresponds to the carotid artery pressure. Its pulse waveform usually oscillates between 80-120 mmHg in a healthy individual [23] and is identified by a first, large peak followed by a second, more subtle one. The pressure at the exit of the last compartment,  $p_{jug}$ , corresponds to the jugular vein pressure and was assumed to be a flat signal of 3 mmHg, with no amplitude. The pressure within all blood compartments between the entrance and exit of the system, as well as the pressure of the brain and CSF cavities, would be somewhere between these two (carotid and jugular pressures).

## FLOW

Arteries, capillaries and vessels in the circulatory system follow the same fluid mechanics as a closed pipe-like conduit. Blood flow is generally laminar, although it can become turbulent in the ascending aorta, when arteries branch and in some pathologic conditions (stenosis, atherosclerosis, etc.) [30]. The model here will assume laminar flow of an incompressible, Newtonian fluid governed by the Poiseuille law. This fluid is subjected to the pressure drop explained above, generating a constant, unidirectional flow across the circulatory system. On the other hand, the influx and efflux of blood into and out of the head forces an analogous oscillatory flow of CSF between the cranial and spinal subarachnoid spaces, as explained in the INTRODUCTION section. This CSF flow occurs through the foramen magnum and is strongly coupled to the heart cycle.

## VOLUME

The vessels and compartments within the cranial vault need to adapt to the constant changes in pressure and flow mentioned above. This adaptation is achieved by the expansion or compression of the different spaces. Additionally, the changes in volume are governed by the Monroe–Kellie doctrine [31]. This principle states that the total volume of intracranial compartments must stay constant due to the constraints imposed by the rigid skull. As a consequence, an increase in the volume of blood, CSF or brain tissue must be compensated for by a decrease in the volume of the other two. The only exception in this model to the Monroe–Kellie doctrine is the spinal SAS, which is located out of the head but connected to the cranial SAS.



## TEMPORAL NORMALIZATION

In order to operate pressures, flows and volumes together, a consistent time frame shared by all magnitudes was needed. To simplify this task, the temporal axis was normalized and all data were expressed as percentages of the CC. Due to its easy identification, a usual reference for the initial state  $t = 0$  is the time of the R wave peak detected in a heart electrocardiogram (ECG). Thus, all signals were shifted to coincide with this reference. However, time acquisition in the DICOM files used in the thesis was expressed in terms of an ECG measured at the finger. The zero-time reference had to be corrected using the heart-to-finger pulse transit time, which has a value around 220 ms [32], to estimate the moment of the R wave peak corresponding to the MR images.

## ASSUMPTIONS AND SIMPLIFICATIONS

Since the model developed for this thesis is a compartmental model, the different cranial and spinal cavities were considered as *conceptual* spaces whose volume can change according to the amount of matter entering or exiting. Therefore, there was no need to define the real-life shape and geometry of the cavities, which highly simplifies the system and reduces the computational needs.

Depending on the model complexity, the number of compartments can vary. For example, the whole arterial tree inside the head can be thought of as a single compartment with homogeneous elasticity. Alternatively, arteries and arterioles can be two different compartments, each of them with their own elasticity. Both examples are of course general approximations to the real case. The more compartments included, the more detailed the model would be, but the computation time would be longer and the results may not vary significantly. During the development of the model, several levels of simplifications were proposed and studied.

On another note, fluid exchange across permeable membranes occurs at a very slow rate compared to blood flow or CSF oscillatory motion. Therefore, processes like CSF production and reabsorption or fluid seepage through capillaries do not significantly affect the dynamics of the system and were neglected.

Finally, the influence of respiration on CSF flow was also neglected. While research suggests that CSF pulsatile motion is dominated by the cardiac pulse wave, breathing still has a mechanical effect on the different pressures and compliances in the thoracic cavity [33]. However, these effects were considered non-important in this study.

### 2.1.3. General equations

The compartmental model of intracranial pulsatility is governed by three balance equations: pressure drop, compartment distensibility and flow continuity. These three equations were applied to different compartments or vessels within the head. An additional constraint on the intracranial volume was imposed by the Monroe–Kellie doctrine. The variables of the model.



pressure, flow and volume are named as  $p(t)$ ,  $q(t)$  and  $v(t)$ , respectively. Lowercase letters are reserved to identify variables in the time domain, while uppercase letters denote constants or variables represented as Fourier coefficients in the frequency domain. A visualization of the equations applied to a vessel or compartment is provided in the three diagrams of [FIGURE 2.2](#).

#### PRESSURE DROP

The flow of fluid through vessels can be modeled after the simplified Hagen–Poiseuille law, where the pressure drop  $\Delta p(t)$  from point *I* to point *II* in a vessel is linearly proportional to the resistance of the vessel  $R$  and the flow between the two points  $q(t)$ . This equation accounts for the momentum balance.

$$\Delta p(t) = p_I(t) - p_{II}(t) = Rq(t) \quad (2.1)$$

This resistance  $R$  is specific for each vessel and depends on the vessel radius and length, fluid viscosity and other factors. Higher resistance leads to a decreased flow. [EQUATION 2.1](#) is implemented on a vessel connecting two compartments, while the other two equations explained below are applied to a compartment itself.

#### COMPARTMENT DISTENSIBILITY

Cavities in our body are usually distensible, meaning that they can expand and compress their volume as a consequence of changes in pressure. The volume of a given compartment  $v(t)$  is regulated by the difference in pressure between the lumen ( $p_{in}(t)$ , within the compartment) and the surrounding space ( $p_{out}(t)$ ), the compliance of its wall tissue  $C$ , and the volume at rest  $V_0$  (the compartment volume when pressure is the same inside and outside).

$$p_{in}(t) - p_{out}(t) = \frac{v(t) - V_0}{C} \quad (2.2)$$

Compliance is the ability of an elastic cavity or organ to easily increase its volume [\[34\]](#) in the presence of a transmural pressure (i.e., across the walls of the cavity). It is a term used to express how much a change in pressure will result in a change in volume. Higher compliance indicates flexibility, while a low compliance is synonymous with stiffness.

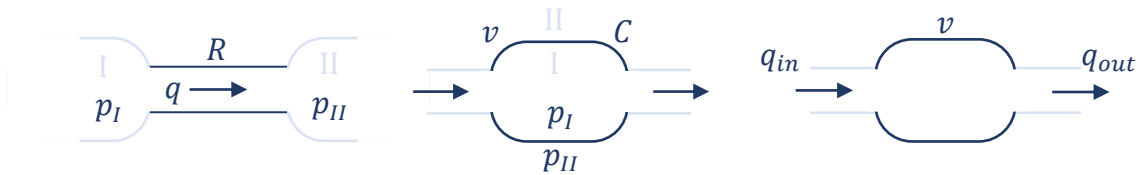


**Figure 2.2. Diagrams depicting the general equations.** The three general equations ([EQS. 2.1–2.3](#)) used in the model are visualized together with the variables involved: pressure drop (left), compartment distensibility (middle) and flow continuity (right).

## FLOW CONTINUITY

The two fluids involved in the model, blood and cerebrospinal fluid, are incompressible. In a closed system, this means that blood and CSF cannot be gained or lost, but instead their volume must stay constant throughout the system. In the model presented here, blood flow at the entrance and exit of the circulatory system are the only way of increasing and decreasing fluid volume. CSF is completely enclosed by the SAS and its volume does not change. Moreover, when fluid enters a compartment, the volume of this compartment must increase in the same proportion in order to fit the fluid inside. This relationship (and the analogous situation of fluid exiting a compartment) can be expressed with the following equation:

$$\frac{dv(t)}{dt} = q_{in}(t) - q_{out}(t), \quad (2.3)$$

where  $\frac{dv(t)}{dt}$  is the change in volume of the compartment along time, and  $q_{in}(t)$  and  $q_{out}(t)$  are the flow entering and exiting the compartment, respectively. Here the effects of fluid seepage, CSF production/absorption and capillary exchange are neglected.

## MONRO–KELLIE DOCTRINE

As mentioned before, the Monro–Kellie doctrine states that the volumetric sum of all intracranial compartments must be constant, so that an increase or decrease in one compartment must be compensated for by the others. Depending on the level of simplification, the Monro–Kellie equation may include some or all of the following anatomical compartments: arteries, arterioles, capillaries, venules, veins, cranial SAS and brain tissue. The only cavity not included is the spinal SAS because it is located in the thorax and is not limited by the rigidity of the skull.

$$\sum_{i=1}^N v_i(t) = V_{tot} \text{ (constant)} \quad (2.4)$$

### 2.1.4. Specific equations

The general equations were implemented to specific cavities inside the skull, specifying to which compartment the pressures, volumes and flows belonged. The number of compartments in the model will depend on the degree of detail we expect from the simulations. The arterial and venous vascular trees, the cranial and spinal SAS, and the brain are essential cavities that need to be included. However, capillaries, arterioles and venules, as well as the specific CSF chambers within the brain (lateral, third and fourth ventricles) can also be considered as independent spaces with their own pressure and volume. Following the interests of this project, no more than six compartments were included. Nonetheless, three variations of the model featuring different degrees of simplification were tested and their

results compared in order to assess the relevance of these assumptions on the model. Refer to [FIGURE 2.3](#) for a visual representation of the compartments and the proposed model configurations.

**Table 2.1. Nomenclature of anatomical structures.** The abbreviations used in equations to name the different anatomical structures are provided. For example,  $p_{car}$  will refer to pressure in the carotid artery (CAR) and  $R_{vnl}$  means the resistance of venules (VNL). Third column indicates if the structure is a compartment, passage or a reference point.

Abbreviation	Anatomical description	Type
ART	Arterial vascular tree inside the cranium.	Compartment
CAP	Capillary bed inside the cranium.	Compartment/Passage
VEN	Venous vascular tree inside the cranium.	Compartment
CRA	Cranial subarachnoid space.	Compartment
SPI	Spinal subarachnoid space (out of the cranium).	Compartment
BRA	Brain tissue, assumed to occupy all space within the cranium that is not a blood- or CSF-filled compartment.	Compartment
ARL	Arterioles connecting arteries to capillaries.	Passage
VNL	Venules connecting capillaries to veins.	Passage
SAS	Subarachnoid space passage connecting cranial and spinal SAS.	Passage
CP BR	Passage from capillaries to brain tissue.	Passage
CR BR	Passage from cranial SAS to brain tissue.	Passage
CAR	Carotid artery, right before entering the cranium.	Reference
JUG	Jugular vein, right after exiting the cranium.	Reference
OUT	Space surrounding the spinal cord, out of the model boundaries.	Reference

#### VARIABLE NOMENCLATURE

Since various models were to be tested, a consistent nomenclature to name the variables was used, both in the equations and in the MATLAB script. Abbreviations in [TABLE 2.1](#) were employed to specify the anatomical compartment or passage where equations were acting on. The table also contains some reference points that were required to provide context to the model: carotid and jugular pressures are located at the entrance and exit of the model's blood vessels, respectively. These two pressures connect our model to the rest of the circulatory system, which is necessary because the whole dynamics are driven by the heartbeat. Additionally, pressure surrounding the spinal cord (identified as  $p_{out}$ ) is also provided as it will affect the expansion and compression of the spinal cavity. On the other hand, pressure out of the cranial cavity is not necessary because the skull is assumed to be a rigid compartment and pressure outside does not affect the dynamics inside. Reference points are not exactly within the model, but rather act as boundaries of it.

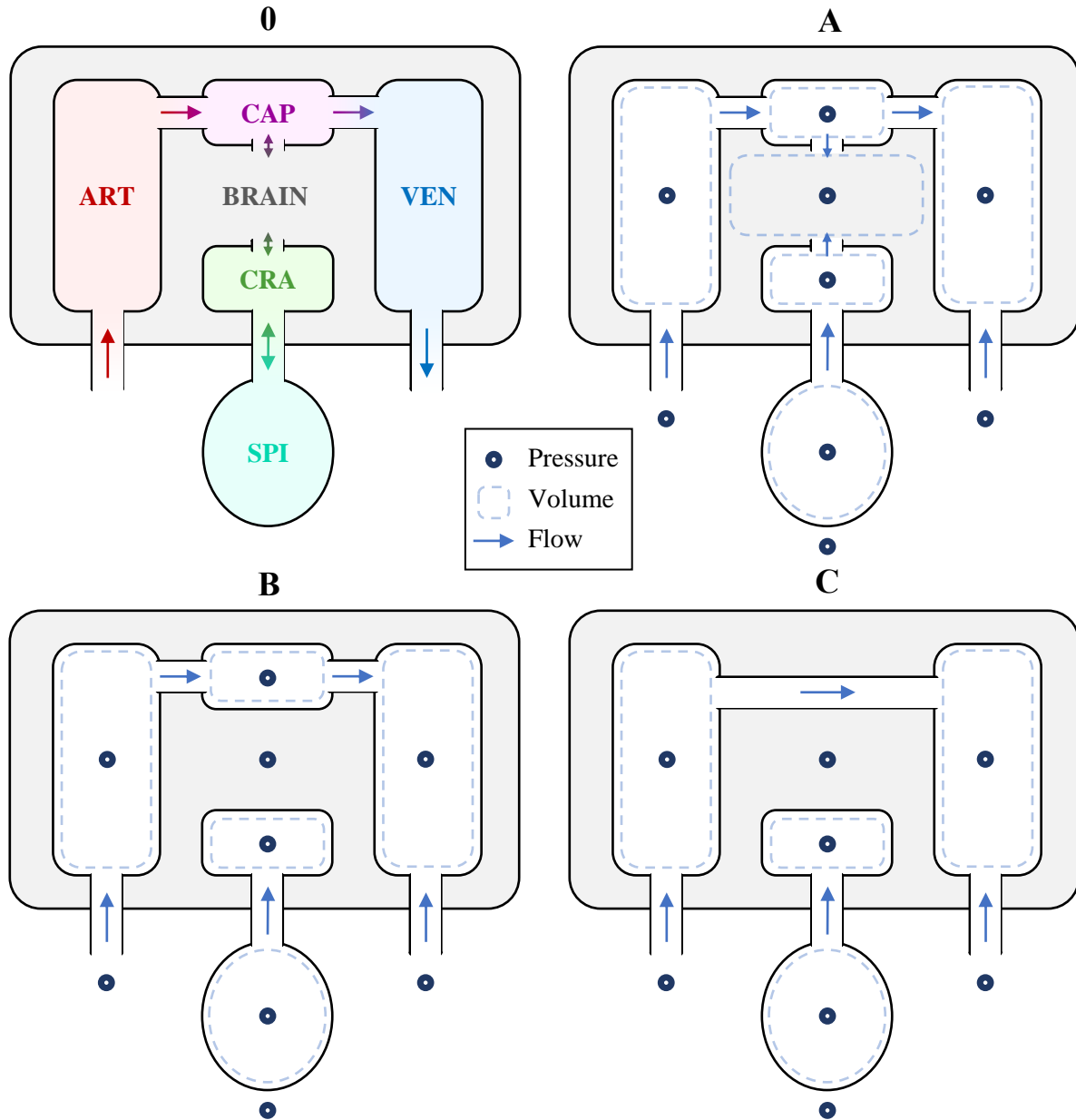


**Figure 2.3. Diagrams of the tested models.** (O) Diagram of the compartments included in the model and the flows between them: arteries, capillaries, veins and CSF-filled spinal and cranial SAS. The gray square represents the brain enclosed by the skull. (A–C) Model variations tested in this project, with different assumptions and simplifications, and with all the pressures (circles), volumes (dotted shapes) and flows (arrows) involved indicated.

#### MODEL VARIATIONS

The original configuration proposed to study intracranial pulsatility was model A in [FIGURE 2.3](#). The six compartments included (arteries, capillaries, veins, cranial SAS, spinal SAS and brain) and the passages connecting them can also be visualized in this figure (diagram O). All compartments except for the spinal SAS are enclosed within the cranium. Blood flows through the vessels driven by a change in pressure between the entrance (carotid artery) and

exit (jugular vein), which are represented with two reference points out of the skull. The influx of blood during systole produces a pulse wave (changes in pressure and volume) that travels through arteries, capillaries and veins. This pulse is also transmitted to the brain and to the ventricles inside it. As explained in the [BIOLOGICAL BACKGROUND](#), once the pulse wave has reached the CSF-filled cavities, the increased pressure will displace part of the CSF volume to the spinal SAS, which is depicted outside and below the skull. All these fluid displacements are represented by arrows in the first diagram (O) of the figure.

Model A incorporates two additional conduits connecting capillaries to the brain, and the brain to the cranial SAS. These passages were included following the hypothesis that a small volume of fluid can enter the interstitial space between brain cells, increasing the total volume of this organ despite the assumption that the tissue itself is incompressible [23]. In contrast, this hypothesis was disregarded in model variation B, where those connections have been removed and therefore brain volume is a constant, rather than a variable. Finally, model C neglects the contribution of capillaries and directly links arteries to veins with a vessel, leading to a five-compartment model and further simplifying the system. While the changes among model variations are not enormous, they should differ enough to produce different outcomes.

## SYSTEM OF EQUATIONS

Once the model was established, general equations ([Eqs. 2.1–2.4](#)) were adapted to each compartment and vessel to formulate the specific equations. Positive flows follow the direction of arrows in [FIGURE 2.3](#) (A–C). As an example, a detailed set of non-linear equations corresponding to model C is given below (equations for models A and B are provided in [ANNEX](#)). Counting the number of pressures, volumes and flows in the depiction of model C will yield a total of 16 variables. Nonetheless, some of these magnitudes do not change in time and can consequently be considered constants. This is the case of reference pressures at the jugular ( $P_{jug}$ ) and outside of the spinal sac ( $P_{out}$ ). As a result, the number of variables in the system is 14 and the number of independent equations, which can be seen in [EQUATION 2.5](#), is 13. As it was explained in [MODEL WORKFLOW](#), this imbalance between equations and unknowns allowed to insert an additional custom equation in the system that would conform the input to the model.

$$\left\{ \begin{array}{lll}
\text{Pressure drop} & \text{Compartment distension} & \text{Flow continuity} \\
\textcircled{1} p_{car} - p_{art} = R_{art} q_{art} & \textcircled{5} p_{art} - p_{bra} = \frac{v_{art} - V_{o,art}}{C_{art}} & \textcircled{10} \frac{dv_{art}}{dt} = q_{art} - q_{cap} \\
\textcircled{2} p_{art} - p_{ven} = R_{cap} q_{cap} & \textcircled{6} p_{ven} - p_{bra} = \frac{v_{ven} - V_{o,ven}}{C_{ven}} & \textcircled{11} \frac{dv_{ven}}{dt} = q_{ven} + q_{cap} \\
\textcircled{3} p_{jug} - p_{ven} = R_{ven} q_{ven} & \textcircled{7} p_{cra} - p_{bra} = \frac{v_{cra} - V_{o,cra}}{C_{cra}} & \textcircled{12} \frac{dv_{cra}}{dt} = q_{sas} \\
\textcircled{4} p_{spi} - p_{cra} = R_{sas} q_{sas} & \textcircled{8} p_{spi} - p_{out} = \frac{v_{spi} - V_{o,spi}}{C_{spi}} & \textcircled{13} \frac{dv_{spi}}{dt} = -q_{sas} \\
\\ 
& \text{Monro- Kellie doctrine} & \\
& \textcircled{9} v_{art} + v_{ven} + v_{cra} = V_{tot} & 
\end{array} \right.$$

(2.5)

### 2.1.5. Equations with Fourier coefficients

Variables involved in the set of equations previously defined (pressure, volume and flow) were expressed as complex Fourier coefficients, fulfilling [EQUATION 2.6](#) (more information on the reasons behind this change can be found in [FOURIER COEFFICIENTS](#)). In frequency domain, these variables are expressed as  $P_n$ ,  $Q_n$  and  $V_n$ , where  $n$  determines the frequency mode number. An example of how to adapt an equation when its variables are transformed into Fourier coefficient form is provided with the general pressure drop equation ([Eq. 2.1](#)).

$$X(t) = \sum_{n=0}^N X_n e^{in\omega t} \quad (2.6)$$

$$p_I(t) - p_{II}(t) = Rq(t) \Rightarrow \sum_n P_n^I e^{in\omega t} - \sum_n P_n^{II} e^{in\omega t} = R \sum_n Q_n e^{in\omega t}$$

Modes range from  $n = 0$  to  $n = 8$ , so that each summation in the above equation can be decomposed as the sum of nine exponentials ( $e^0, e^{i\omega t}, \dots, e^{8i\omega t}$ ). In order to fulfill the equation, each mode must be independently fulfilled in a separate equation. When expressing each mode separately, one realizes that the exponentials cancel out, resulting in a linear relationship between the Fourier coefficients.

$$\begin{cases} P_0^I e^0 - P_0^{II} e^0 = RQ_0 e^0 \\ P_1^I e^{i\omega t} - P_1^{II} e^{i\omega t} = RQ_1 e^{i\omega t} \\ \vdots \\ P_8^I e^{8i\omega t} - P_8^{II} e^{8i\omega t} = RQ_8 e^{8i\omega t} \end{cases} \Rightarrow \begin{cases} P_0^I - P_0^{II} = RQ_0 \\ P_1^I - P_1^{II} = RQ_1 \\ \vdots \\ P_8^I - P_8^{II} = RQ_8 \end{cases}$$

Expressing these new formulas in a vectorial form, the pressure drop equation can be rewritten as follows:

$$P_n^I - P_n^{II} = RQ_n \quad (2.7)$$

where  $X_n$  is the column vector containing the complex Fourier coefficients of signal  $X(t)$ . Analogously, the compartment distensibility equation can be rewritten in a similar manner, with the only addition of introducing a constant term,  $V_0$ , that is not multiplied by any variable. This independent term will only affect the zeroth mode, where the exponentials are reduced to one ( $X_0 e^0 = X_0$ ). [EQUATION 2.2](#) can then be expressed in vectorial form, where  $V_0$  is a vector containing the value of volume at rest in the first position (corresponding to the zeroth mode) and zeros in the other eight elements. Notice that the compliance term  $C$  has been relocated to the opposite side of the equation as a preliminary step to prepare the expression for the forthcoming matrix form of the system in the code.

$$CP_n^{in} - CP_n^{out} = V_n - V_0 \quad (2.8)$$

The presence of a time derivative in the flow continuity equation ([EQ. 2.3](#)) makes it also a special case where some additional terms may appear. When  $v(t)$  is expressed as a sum of exponentials, the derivative becomes:

$$\frac{dv(t)}{dt} = \frac{d}{dt} \left( \sum_{n=0}^N V_n e^{in\omega t} \right) = \sum_{n=0}^N \frac{d}{dt} (V_n e^{in\omega t}) = \sum_{n=0}^N in\omega \cdot V_n e^{in\omega t}$$

Using this new term and following the same procedure than for the previous two equations, the continuity equation can be rewritten as:

$$in\omega V_n = Q_n^{in} - Q_n^{out} \quad (2.9)$$

Therefore, the three general equations have been expressed with Fourier coefficients and simplified, yielding a set of linear equations with no exponentials and no time derivatives. These new expressions ([EQUATIONS 2.7–2.9](#)) were implemented at different vessels and compartments to obtain a mathematical representation of intracranial dynamics. Together with the Monro–Kellie doctrine (expressed below with Fourier coefficients), the new formulas were used to rewrite the system of equations presented in [EQUATION 2.5](#).

$$\sum_{i=1}^N V_n^i = V_{tot} \quad (2.10)$$

### 2.1.6. Code implementation

The model was programmed using MATLAB. Values of volume at rest, resistance and compliance were initially set according to literature, mostly based on data proposed by Linninger *et al.* [\[23\]](#). Some of these values were modified in an attempt to understand their importance in the overall dynamics. The same source also provided a function for the carotid

pressure that could serve as input. Constant pressure values were also given for the jugular pressure and pressure outside of the spinal cavity. The total volume used in the Monroe–Kellie equation is the sum of all volumes at rest. Finally, flows extracted from MR images were also available as input. Pressures, volumes, flows, resistances, compliances and volumes at rest were defined as MATLAB structures where each field corresponded to a different anatomical part (e.g., `P.car` for the pressure in the carotid artery).

**Table 2.2. Order of variables in the system matrix.** The order used to sort columns in matrix  $A$  and variables in the output vector  $X_n$  is presented in this table. Pressure signals are sorted first, followed by volumes and ending with flows. The meaning of each abbreviation can be consulted in [TABLE 2.1](#). ART and VEN referring to flow (and resistance) correspond to blood flows at the entrance and exit of the model, respectively.

<b>Pressure</b>	CAR	ART	CAP	VEN	CRA	SPI	BRA
<b>Volume</b>	ART	CAP	VEN	CRA	SPI	BRA	
<b>Flow</b>	ART	ARL	VNL	VEN	SAS	CP BR	CR BR

Since each frequency mode needs to be fulfilled independently of the others, a `for` loop was defined to iterate through all modes and solve them separately. An implementation of model C in [FIGURE 2.3](#) is provided in the code below. The set of frequency-domain equations was expressed in matrix form  $AX = B$ , which MATLAB can easily solve in one single command:  $X_n = A \setminus B$ . Matrix  $A$  contained all coefficients of the system and vector  $B$  contained all the independent terms moved to the right-hand side of the equal sign. The output  $X_n$  was a column vector with the predicted behavior of all variables along one CC, sorted in the order specified in [TABLE 2.2](#). This same order corresponds to the columns of matrix  $A$ , while rows correspond to the equations numbered as in [EQUATION 2.5](#). The matrix in the code was separated into three blocks of rows for an easier visualization: the first one contains pressure drop equations, the second one includes the compartment distension and Monroe–Kellie equations, and the last block incorporates flow continuity as well as the input.

Because the independent terms in vector  $B$  are constant and not multiplied by any exponential, they are only involved in the zeroth mode where the exponential is cancelled. Hence,  $B$  was initially defined as all zeros and then an `if` condition was used to set the constant terms only at the zeroth mode. On a different side, variables `inputA` and `inputB` were used to introduce the additional equation that provided the input to the model. After solving the system and obtaining the Fourier coefficients of the simulated variables, signals were reconstructed in time domain for a few cycles and displayed through graphs for their comparison and analysis, which will be discussed in the section [RESULTS AND DISCUSSION](#).



```

% Solving the unknowns of the model
for n = 0:N-1 % 0 to 8
    inw = li*n*w;

    A = [... % coefficients of the system
        1 -1 0 0 0 0 0 0 0 0 -R.art 0 0 0 ;...
        0 1 -1 0 0 0 0 0 0 0 0 -R.cap 0 0 ;...
        0 0 -1 0 0 0 0 0 0 0 0 0 -R.ven 0 ;...
        0 0 0 -1 1 0 0 0 0 0 0 0 0 -R.sas;...

        0 C.art 0 0 0 -C.art -1 0 0 0 0 0 0 0;...
        0 0 C.ven 0 0 -C.ven 0 -1 0 0 0 0 0 0;...
        0 0 0 C.cra 0 -C.cra 0 0 -1 0 0 0 0 0;...
        0 0 0 0 C.spi 0 0 0 0 -1 0 0 0 0;...
        0 0 0 0 0 0 1 1 1 0 0 0 0 0;... %MK doct.

        0 0 0 0 0 0 inw 0 0 0 -1 1 0 0;...
        0 0 0 0 0 0 0 inw 0 0 0 -1 -1 0;...
        0 0 0 0 0 0 0 0 inw 0 0 0 0 -1;...
        0 0 0 0 0 0 0 0 0 inw 0 0 0 1;...
        inputA];

    B = [zeros(1,13) inputB]'; % independent terms of the system

    % Constants only affect the mode zero (n=0)
    if n==0
        B = [ 0 0 -Pjug 0 ...
            -Vo.art -Vo.ven -Vo.cra C.spi*Pout-Vo.spi Vtot ...
            0 0 0 0 inputB]';end

    Xn = A\B; % unknowns of the system, Xn = [Pn Vn Qn]
end

```

## 2.2. Model study

After having successfully implemented the model, a new part of the study was conducted to compare model variations and to modify matrix coefficients in an effort to improve the resulting output. By this process, the physiological parameters of the internal structures can be estimated. In addition, an attempt was made to identify and extract possible flow and pressure parameters to link with CSF-related disorders. The discussion of the results is reserved for the section dedicated to that purpose.

### 2.2.1. Comparison of model variations

The three model variations proposed in this thesis were tested and compared. To do so, the same input was introduced to all models and then all output variables were plotted for a detailed comparison (FIGURE 3.1). The input chosen for this task was a pulse waveform representing the carotid artery pressure ( $p_{car}$  in the equations and `P.car` in the code) because it represents the physiological driving force at the entrance of the system. This pressure signal was obtained from a research paper [23] that directly provided the Fourier

coefficients to represent the signal. After comparing the output of all systems, the simplest variation (model C) was selected to be used in the following part of the study. The reasons behind this decision are explained in the [RESULTS OF MODEL COMPARISON](#) section of the discussion. A detailed representation of this model, including the names of all pressures, volumes and flows, is provided in [FIGURE 2.4](#).

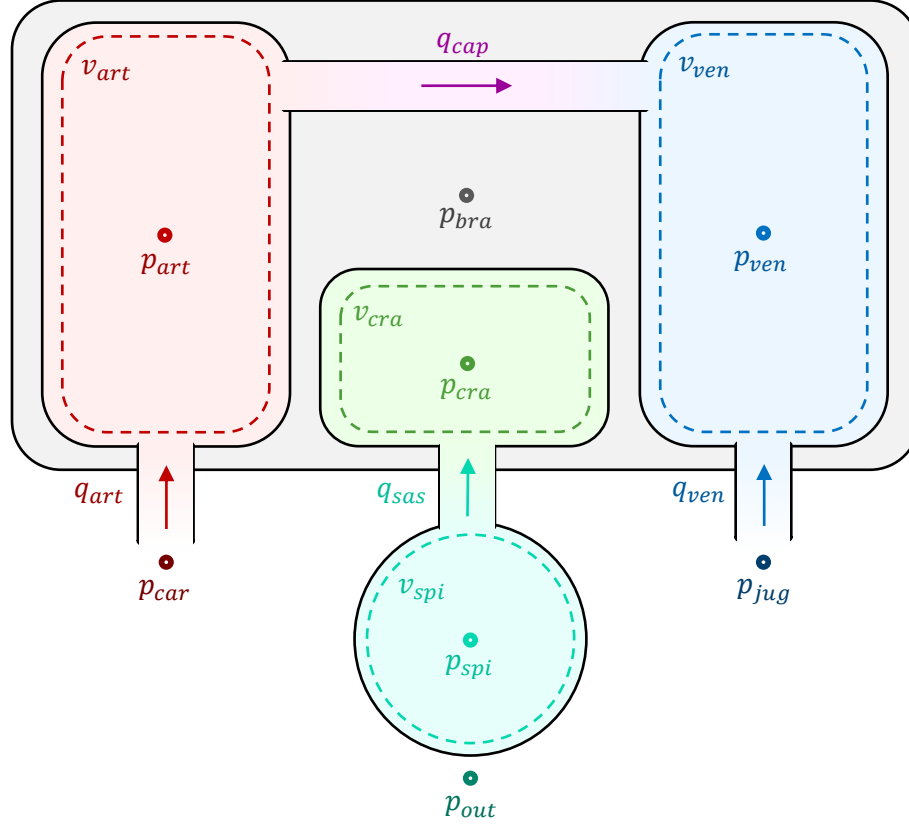


**Figure 2.4. Detailed diagram of model C.** All pressures ( $p_i$ ), volumes ( $v_i$ ) and flows ( $q_i$ ) are indicated and colored according to the structure they belong to. This model was the simplest among the three variations, amounting up to 14 variables ( $p_{jug}$  and  $p_{out}$  are constants). Each vessel flow has a resistance associated to it, while compartments are characterized by their volume at rest and compliance.

### 2.2.2. Tuning of matrix coefficients

The matrix coefficients in the mathematical equations governing the system dynamics (both in the matrix A and the vector of independent terms B) are a combination of resistance, compliance, volume at rest and pressure values assumed to be constant. The initial values assigned to all these magnitudes, which can be consulted in [TABLE 2.3](#), were mostly based on published research: the carotid resistance was obtained from Zhang *et al.* [35], cranial-spinal passage resistance from Støverud *et al.* [36], and all other resistance values from Sorek *et al.* [20]. Compliances and volumes at rest were retrieved from Linninger *et al.* [23]. However, it should be noted that applying statistical values derived from other studies to analyze the subject-specific images acquired for *this* model would not accurately replicate the real fluid dynamics of the subject. To ensure a faithful representation, these parameters needed to be

adapted to match the biological properties of the individual. By doing so, these physiological features would be estimated and pathology indicators could potentially be identified.

**Table 2.3. Values used for constant parameters.** Initial values (except when “estimated” is said) were obtained from published material, final values were manually adjusted. Two values indicate that a range was provided in the literature, while a dash in the *final value* column is written in constants that were not evaluated (because they were not present in model C).  $R_{art}$  and  $R_{ven}$  are the internal carotid and jugular resistances, which were used for the entrance and exit of blood circulation in the model.

	Parameter	Initial value	Final value	Source
<b>Volume at rest (cm<sup>3</sup>)</b>	$V_{o,art}$	30–46	30	Linninger
	$V_{o,cap}$	20	—	Linninger
	$V_{o,ven}$	60	60	(Estimated)
	$V_{o,cra}$	45–50	47.5	Linninger
	$V_{o,spi}$	90–100	95	Linninger
	$V_{o,bra}$	1400	—	Linninger
<b>Compliance (cm<sup>3</sup>/mmHg)</b>	$C_{art}$	0.0147	0.025	Linninger
	$C_{cap}$	$6.06 \times 10^{-3}$	—	Linninger
	$C_{ven}$	0.0293–0.16	0.040	Linninger
	$C_{cra}$	0.0792–6.33	0.725	Linninger
	$C_{spi}$	0.0127	0.0220	Linninger
	$C_{bra}$	18.7–187	40	Linninger
<b>Resistance (mmHg s/cm<sup>3</sup>)</b>	$R_{art}$	1.40	1.40	Zhang
	$R_{arl}$	5.60	56	Sorek
	$R_{vnl}$	1.68	1000	Sorek
	$R_{ven}$	0.558	0.4	Sorek
	$R_{sas}$	0.045–0.06	3.75	Støverud
	$R_{cp br}$	$8 \times 10^5$	—	Sorek
	$R_{cr br}$	800.3	—	Sorek
<b>Pressure (mmHg)</b>	$p_{jug}$	3	3	Linninger
	$p_{out}$	10	10	(Estimated)

The procedure to tune these constants was done by choosing one specific parameter, defining around five possible values for it, and testing model C with each of those values. Arterial flow measured from the MR images was used as the input to the model, which then would simulate the behavior of all other variables. Finally, the simulated CSF flow was compared to the experimental CSF signal obtained by MRI. The value that yielded the most similar prediction of this signal was selected to become the new weight of the parameter. Similarity was visually assessed (FIGURE 3.2) but the sum of absolute differences (EQUATION 2.11) was also computed to provide a mathematical measure. Different orders of magnitude were

used in the first tuning round and whenever significant changes were observed in the signal simulation, a second finer tuning was done with more precise values. If modifying the parameter did not affect the simulation, then no further tuning was realized. After applying the whole tuning process for all constants, the final values obtained were annotated in [TABLE 2.3](#).

$$SAD = \sum_t |q_{sas}^{exp}(t) - q_{sas}^{sim}(t)| \quad (2.11)$$

### 2.2.3. Study of pathological conditions

Initially, the intention of testing the model with clinical data was manifested in an attempt to identify parameters, either related to CSF pulsatility or to mechanical properties of the compartments, which could be linked to different pathologies and therefore serve as diagnostic indicators. However, the regulation to protect the patient's privacy imposes some restrictions to the access of health data and medical images (more information on [LEGISLATION ANALYSIS](#)). As a consequence, the desired MR images were not obtained and this objective could not be fulfilled as part of this thesis. Still, the possibility remains open for future research using the model developed here.

## 2.3. Data acquisition and processing

As a previous step to building the model, real data were derived from magnetic resonance imaging (MRI) for their use in the model creation. Medical images from a healthy individual were obtained by phase-contrast MRI. CSF and blood flows were then extracted from them and used in the development of the computational model. The context of data acquisition and the steps followed to process the images are explained below. Some parts of the MATLAB script used in the data processing are provided. These code fragments have been adapted and simplified for clarity purposes.

### 2.3.1. Image acquisition

MRI uses strong magnetic fields and radio waves to generate detailed images of the body's internal structures. Phase-contrast MRI is often used in clinical applications due to its non-invasiveness, high spatial resolution, quantitative output and ability to provide a direct measurement of velocity and flow direction. It can aid in the diagnosis of heart valve disease by measuring cardiac blood flow, and also in neuroimaging by measuring CSF flow for the assessment of normal pressure hydrocephalus and Chiari malformation type I [\[37\]](#). The MR images used in the study were obtained from a healthy subject at *Centro de Investigación Mente, Cerebro y Comportamiento*<sup>1</sup>, a research facility in University of Granada, Spain. These images corresponded mainly to axial planes of the subject taken at relevant locations,

---

<sup>1</sup> More information on their website <https://cimcyc.ugr.es>.

particularly at the level of the axis vertebrae (C2) in the neck. This section allows to capture the velocity of the two fluids near the foramen magnum through which blood and CSF enter and exit the head.

In phase-contrast MRI, a parameter called velocity encoding (VENC) is set prior to acquisition. This parameter influences how the magnetic fields will be applied during the imaging process, and it determines the maximum velocity that can be measured. Different values of VENC may be used on the same subject to obtain a wide range of velocities with high precision. With such objective in mind, three series using VENC equal to 10, 30 and 80 cm/s were obtained for each patient. This produced redundant data that would later be combined (details on [ALIASING REMOVAL](#)). Each series contained 30 timeframes that together provided enough data points to reconstruct velocities along the CC with good resolution. Since MRI returns two images per acquisition time (phase and magnitude), a total of 60 images per series was obtained. Phase and magnitude images are complementary and can be combined into a single picture representing the internal anatomy and physiology of our bodies. All these images were stored as DICOM files.

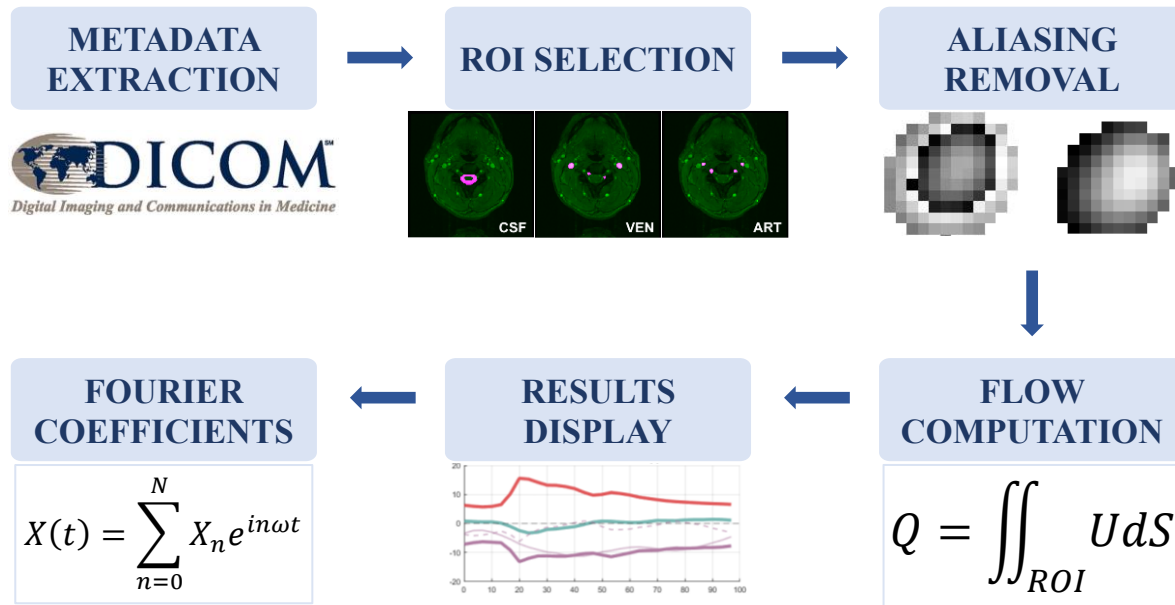


**Figure 2.5. Steps in the process of flow extraction.** In order to obtain flow information for each region from the MR images, the script in MATLAB followed these six main phases implemented by different functions. Images produced by the MATLAB code, except for the DICOM logo [38].

The acquired images contained the necessary data to extract velocity information. However, our fluid dynamics model required blood and CSF *flow* data, rather than absolute velocities, in order to predict CSF flow oscillations and motion. On top of that, only the flow through regions of interest was needed. For those reasons, the images had to be processed to derive flow information from them. This objective was accomplished through a series of steps, illustrated in [FIGURE 2.5](#), that were implemented using several MATLAB functions partially developed by supervisor Prof. Wilfried Coenen. As part of the thesis, those functions were

further elaborated to obtain the desired results, as well as to improve performance and code readability.

### 2.3.2. Metadata extraction

The first step to process the MRI images was to extract relevant information from the DICOM files. DICOM is an international standard for communication of biomedical digital images. It defines both an information model (format and structure used to store data) and services (communication protocols used to exchange data between different devices or systems) [39]. Medical images stored with the DICOM information model include the image itself plus all metadata related to the patient, acquisition, image device, etc. All this information can be easily extracted using the MATLAB function `dicominfo`, which returns a structure where each field corresponds to a DICOM attribute. The image, trigger time and flag indicating phase/magnitude were obtained for each file. Some additional information common for all time instants was also collected, such as the duration of the CC, the velocity encoding and the pixel area, among others.

Once the data was gathered, an additional step was taken to calculate the velocity field at each time instant. The two types of images produced by an MRI scanner, phase (`phase`) and magnitude (`magni`), correspond to different aspects of the behavior of protons inside our body and they can be combined to generate a unified picture representing the velocity ( $U$ ) of tissues or fluids at each pixel. The code lines below show how this operation was done for each series  $s$  and time instant  $t$ . The 60 images of each series were sorted by flag and trigger time in order to have all magnitude images ordered by acquisition time (1–30) followed by the phase images (31–60). After this step, each series would consist of 30 frames ordered along the CC, containing the desired velocity data.

```
% Convert the phase and magnitude images into velocity field
[~,j] = sortrows([flag{s}, trigger_time{s}], [1 2]);
img{s} = img{s}(j);

for t = 1:30
    magni{s}{t} = img{s}{t};
    phase{s}{t} = img{s}{t+30};
    U{s}{t} = -.1*(phase{s}{t}./max(magni{s}{t},1))/venc_scaled(s);
end
```

### 2.3.3. ROI selection

A region of interest (ROI) is a subset of pixels (or voxels) within an image that share some property which makes them relevant for further analysis, compared to the pixels not included in the ROI. The attributes defining a ROI may be related to the pixel value, position, texture, change in time or any other significant feature. In the process of extracting flow information, vessels or channels through which blood or CSF was to be measured were considered ROIs. These include arterial vessels (internal carotid arteries, vertebral arteries), venous vessels

(internal jugular veins, epidural veins) and CSF channel (spinal SAS). These nine ROIs (accounting for left and right blood vessels) were manually chosen from one of the images (see [FIGURE 2.6](#)), assuming no tissue motion would happen during acquisition and therefore regions would stay in the same location for all time instants. ROIs were used to extract pixel values representing only our target blood and CSF flow, while ignoring information from the surrounding tissues. In order to do so, the image with all the data was multiplied by a binary matrix containing ones at a specific ROI and zeros otherwise. The output matrix would then contain all zeros except for the chosen region, which would contain blood and CSF velocity data.

```
for s = I.ser % series index
    for r = I.reg{s} % region index
        for v = I.ves{r} % vessel index
            for t = I.tim % time index
                U_roi{r,v}{s}{t} = U{s}{t}.*ROI{r,v}{s};
            end;end;end;end
```

Throughout the script, cell arrays were used to store ROI, velocity, flow and other relevant information. These variables were created with a common structure to organize data according to the series, region (CSF, arteries or veins), vessel and time instant. Organizing cell arrays into those “levels”, which were defined in an index variable ( $I$ ), allowed to unify the workflow and to handle the data using `for` loops. Although `for` loops are not the most computationally efficient option, they do provide a flexible, visually intuitive and straightforward manner of iterating through all dimensions of a variable. Besides, finding an alternative approach would require intricate modifications and adaptations of the code that may result in a more cumbersome and complicated code design.

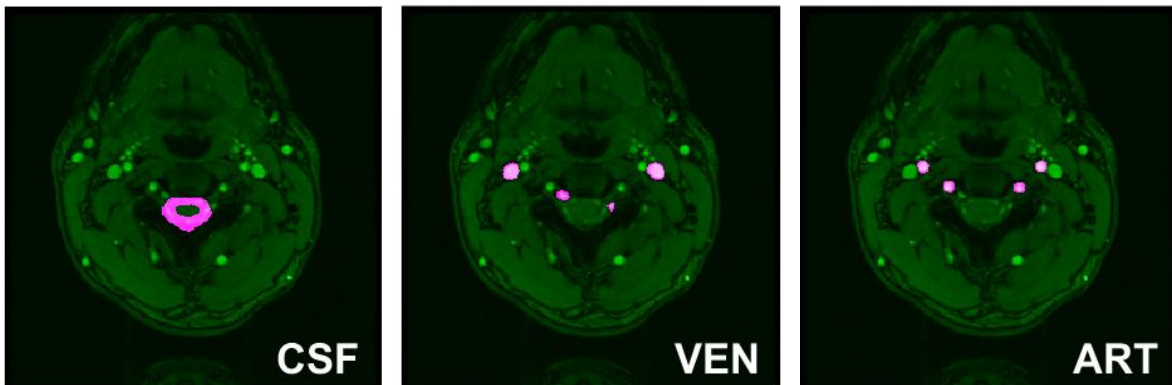


**Figure 2.6. Regions of interest.** ROIs are highlighted in pink on top of the MR images (green). CSF channel (left) corresponds to the spinal SAS surrounding the spinal cord. Venous vessels (middle) include left and right internal jugular and epidural veins. Arterial vessels (right) comprise the left and right internal carotid and vertebral arteries.

A different ROI for each velocity encoding was defined, leading to three equivalent ROIs that were later merged into a combined ROI using one of three approaches: computing the



union of the ROIs, determining their intersection or selecting one of the three ROIs as representative. The purpose of combining ROIs was to enable comparison between the different series and remove aliasing. Using the union ensured that the vessel was completely included within the ROI, while the intersection guaranteed the exclusion of surrounding tissue that might interfere with the results. Alternatively, choosing the ROI from a specific series may be useful when aliasing does not occur, allowing to use the values of one series without considering the others.

### 2.3.4. Aliasing removal

Velocity encoding establishes the upper and lower limits of fluid velocity that can be quantified. Once velocity information is extracted, pixel values in the image are bounded to the range  $[-VENC, +VENC]$ . This range is periodic and “circular” in the sense that crossing beyond one of the limits will lead to the opposite limit, as it is illustrated in [FIGURE 2.7 \(A\)](#). This means that if the real velocity is below or above  $\pm VENC$ , pixel values will still be matched to this range in a process known as phase wrap [\[40\]](#). As an example: if VENC is set to 10 cm/s, data will be expressed as a value between  $-10$  and  $+10$ . The negative range from  $-30$  to  $-10$  and the positive range from  $10$  to  $30$  will both also be matched to the range  $\pm 10$ . Therefore, if the real velocity for a certain pixel is 12 cm/s, the value returned by the machine will be  $-8$  cm/s, and if the real velocity is  $-12$  cm/s, the value appearing in the results will be 8 cm/s (see the figure for a visual representation of this example). This distortion is known as velocity aliasing and poses a problem when extracting and interpreting information. Examples of velocity mismatch at different blood vessels are also provided in [FIGURE 2.7 \(B\)](#).

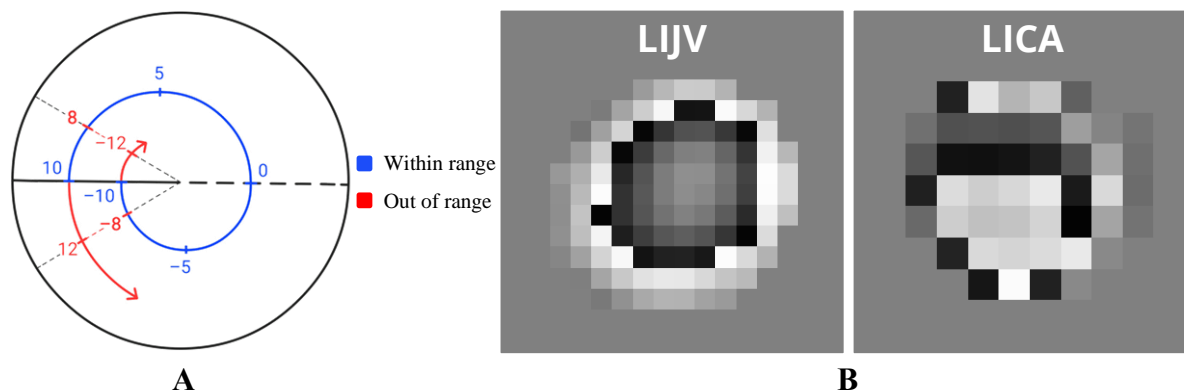


**Figure 2.7. Velocity mismatch due to encoding velocity constraints.** (A) A velocity encoding range of  $\pm 10$  cm/s (blue spiral) is depicted. When real values exceed the range (i.e., 12 and  $-12$  in red), they are matched to their equivalent value within the range, according to their angle ( $-8$  and 8, respectively). (B) Examples of velocity mismatch in the *left internal jugular vein* (LIJV) and *left internal carotid artery* (LICA). Lighter pixels indicate values near the range upper limit, and vice versa. In both vessels, a smooth velocity field should be observed across all the ROI, but instead there are “jumps” (sudden changes) which indicate that real values fall above or below the range. The jump in LIJV is evident and could be manually fixed, while the jumps in LICA are not so evident and a specialized algorithm is needed to fix them.



A straightforward option to avoid aliasing is to choose a VENC large enough to ensure that real velocity values will not exceed it. Nonetheless, using a large VENC has the disadvantage of obtaining less precise measurements with a lower velocity-to-noise ratio [41]. Conversely, selecting a smaller VENC will provide greater precision at the expense of increasing the probability of aliasing. In order to achieve the benefits of both options, it is common to perform multiple acquisitions with different velocity encodings, and then combine the results to generate an image with high precision that also covers a wide range of velocities [42]. For this project, up to three VENC of 10, 30 and 80 cm/s were used. An algorithm was developed to match the values of the lowest VENC—the most precise measurement but bounded to a  $\pm 10$  range—to their correct range according to a higher VENC.

```
% Remove aliasing - VEN and ART
venc=[10 30 80]; % velocity encoding (VENC) values
vLO=-8*venc(1):2*venc(1):8*venc(1); % ranges below and above [-10,10] (VENC = 10)
vME=-4*venc(2):2*venc(2):4*venc(2); % ranges below and above [-30,30] (VENC = 30)

for r = I.reg(2:3) % for VEN and ART
    for v = I.ves{r}
        [row,col] = find(ROI{r,v}); % pixel coordinates of ROI

        for t = I.tim
            for k = 1:length(row) %for each pixel in ROI
                rk = row(k);
                ck = col(k);

                [~,ind] = min(abs(U{r,v}{2}{t}(rk,ck) - U{r,v}{3}{t}(rk,ck) + vME));
                U{r,v}{2}{t}(rk,ck) = U{r,v}{2}{t}(rk,ck) + vME(ind);

                [~,ind] = min(abs(U{r,v}{1}{t}(rk,ck) - U{r,v}{2}{t}(rk,ck) + vLO));
                U_corrt{r,v}{t}(rk,ck) = U{r,v}{1}{t}(rk,ck) + vLO(ind);
            end;
        end;
    end;
end;end;end;end
```

The algorithm iterates through each vessel and locates pixel positions belonging to the ROI. Then, for each pixel in the ROI, it finds the most appropriate velocity value ( $U$ ) taking into account the values offered in all series. It should be reminded that VENC defines a range of valid velocity values, but the real one may be one or several ranges “above” or “below” due to phase wrapping. To understand how the correction is achieved, consider the example in [FIGURE 2.7](#) (B, left) where blood velocity in the center of the jugular vein is so high that it exceeds the  $\pm 10$  range. Real values may probably lie within the  $(-30, -10)$  range (since venous flow is negative) and the purpose of the algorithm is to modify the values of the lowest VENC (which lie in the  $\pm 10$  range) to correctly fit them into that  $(-30, -10)$  range by comparing them to data of a higher VENC. This comparison is made by obtaining the difference between the values from the higher VENC and the adjusted values of the lower VENC, and finding the range that minimizes that difference (it should be around zero in the absence of aliasing). [TABLE 2.4](#) presents some examples comparing two velocity encodings to help understand how this algorithm is performed. In the code, `vLO` and `vME` are used to test several ranges above and below the  $\pm 10$  range.

**Table 2.4. Example cases of aliasing removal.** Fictitious measurements using two VENC values (10 and 30) are compared. Five “real” values are provided as reference. The algorithm is used to test three possibilities: the real value falls within the range of the lower VENC ( $n = 0$ ), or either in the immediately upper ( $n = 1$ ) or lower ( $n = -1$ ) range. For each possibility, the value corresponding to the lower VENC ( $U_{V10}$ ) is adjusted with an offset  $\Delta u$  which is twice the lower VENC. The difference between  $U_{V30}$  and the adjusted  $U_{V10}$  is computed, and the range corresponding to the minimum of these differences is selected. In the table, this range is highlighted in black while the other two possibilities appear in light gray.

Real value	Measured values		Algorithm	Final value
	$U_{V10}$	$U_{V30}$	Range n: $(U_{V10} + n\Delta u) - U_{V30}$	
- 22	- 1	- 25	<div> <div>Range -1: <math>(-1 - 20) + 25 = 4</math></div> <div>Range 0: <math>(-1 + 0) + 25 = 24</math></div> <div>Range +1: <math>(-1 + 20) + 25 = 44</math></div> </div> $\rightarrow n = -1$	$-1 - 20 = -21$
- 17	4	- 13	<div> <div>Range -1: <math>(4 - 20) + 13 = -4</math></div> <div>Range 0: <math>(4 + 0) + 13 = 16</math></div> <div>Range +1: <math>(4 + 20) + 13 = 36</math></div> </div> $\rightarrow n = -1$	$4 - 20 = -16$
5	5	6	<div> <div>Range -1: <math>(5 - 20) - 6 = -21</math></div> <div>Range 0: <math>(5 + 0) - 6 = -1</math></div> <div>Range +1: <math>(5 + 20) - 6 = 19</math></div> </div> $\rightarrow n = 0$	$5 + 0 = 5$
12	- 9	13	<div> <div>Range -1: <math>(-9 - 20) - 13 = -42</math></div> <div>Range 0: <math>(-9 + 0) - 13 = -22</math></div> <div>Range +1: <math>(-9 + 20) - 13 = -2</math></div> </div> $\rightarrow n = 1$	$-9 + 20 = 11$
27	7	23	<div> <div>Range -1: <math>(7 - 20) - 23 = -36</math></div> <div>Range 0: <math>(7 + 0) - 23 = -16</math></div> <div>Range +1: <math>(7 + 20) - 23 = 4</math></div> </div> $\rightarrow n = 1$	$7 + 20 = 27$

### 2.3.5. Flow computation

Once the aliasing problem was solved and the three series using different VENC were combined into one, the data to be processed consisted of nine ROIs spanned across 30 timeframes. Flow was then computed for each ROI and timeframe. The formula to obtain the flow of fluid through a surface depends on the velocity of the fluid ( $U$ ) and the total area of that surface ( $A$ ):

$$Q = \iint_A U dA \quad (2.12)$$

In the code, [EQUATION 2.12](#) was implemented by summing the velocity values of all pixels in the ROI and multiplying by the pixel area (PXA). Flows were quantified at individual venous and arterial vessels, as well as at the spinal SAS. The total flow of blood entering the head could be known by summing all arterial flows. Analogously, total venous outflow from the cranial cavity was determined by the summation of flows through all venous vessels. Following the standard convention, cephalic flow (in the direction towards the head) was defined as positive and caudal flow (exiting the head) was identified as negative.

```

% Pulse transit time (PTT) is scaled and added to TIME, and points
% exceeding 100 are moved to the beginning of the vector
deltaT = 220; % PTT from heart to finger (ms)
time = time + 100*deltaT/T;
time(time>100) = time(time>100) - 100;
[time,j] = sort(time);

Q = cell(size(U)); % flow (cm^3/s)
for r = I.reg
    for v = I.ves{r}
        for t = I.tim
            Q{r,v}(t) = sum(U{r,v}{t}(:))*PXA;
        end
        Q{r,v} = Q{r,v}(j);
    end;end
end;end

```

In order to ensure consistent synchronization between pressure, flow and volume signals, a unified time frame was established by normalizing the temporal variable to the CC and setting the zero reference at the R wave peak of the heart ECG. According to the metadata extracted from the DICOM files, the initial temporal point in the MR images was set at the R wave peak measured at the finger. Therefore, flow signals were shifted to make the initial time coincide with the desired zero reference point. To achieve this time shift, the heart-to-finger pulse transit time (PTT) was summed to the DICOM timeline. The PTT is an offset representing the time that the ECG wave requires to travel from the heart to the finger. A value of 220 ms based on the literature [32] was used for this time offset.

### 2.3.6. Results display

Two types of graphs were used to visualize the evolution of flows throughout the CC. Firstly, in order to evaluate the aliasing-removal algorithm, the corrected flow through each individual blood vessel was plotted against time, together with the flows of the different velocity encoding (which may be distorted by aliasing). The resulting diagrams for venous and arterial vessels are shown in [FIGURE 3.3](#). Secondly, the total flows through each region (arteries, veins and SAS channel) were displayed together ([FIGURE 3.4](#)) to help in the study of volume entering and exiting the cranial cavity and CSF pulsatility. Flow signals were repeated in time in order to show a few heart cycles, which facilitates the visualization of the pulse wave. All these charts will be discussed in the [RESULTS AND DISCUSSION](#) section.

### 2.3.7. Fourier coefficients

Once the flows were obtained as a set of data points in time (a temporal signal), a further step was taken to transform them into complex Fourier coefficients multiplied by exponentials, following the expression in [EQUATION 2.6](#) which is also displayed here. The reason for using Fourier coefficients is that the signal can be easily reconstructed as a continuous function in the time domain, providing information even at time instants that were not defined in the original, discrete data set. Another advantage of expressing signals as exponentials is that the

time derivative, which is present in the continuity equation, becomes straightforward (this was discussed before in [EQUATIONS WITH FOURIER COEFFICIENTS](#)). In addition, when the set of equations used in the model are further simplified, the exponentials cancel out resulting in a system of linear equations that can be easily implemented and solved in MATLAB. Finally, this transformation allowed to represent all the involved magnitudes (flow, pressure and volume) with the same mathematical expression, homogenizing the input to the model.

$$X(t) = \sum_{n=0}^N X_n e^{in\omega t} \quad (\text{Eq. 2.6})$$

```
% FOURIERCOEFF returns a column XN with the N first coefficients of the
% Fourier series that is equivalent to the signal X. The number of
% Fourier coefficients must be equal or smaller than the length of the
% signal.
function[Xn] = FourierCoeff(X,t,N,w,t_rec)
N = min(N,length(X)); % number of coefficients
n = (0:N-1)'; % coefficient index
X = fft(X)/length(X); % all Fourier coefficients
Xn = Y(n+1); % first N coefficients
Xn(2:end) = 2*conj(Yn(2:end));

X_rec = real(sum(Xn.*exp(1i*n*w*t_rec))); % reconstructed signal X
end
```

The operation to reproduce any signal  $X(t)$  from its coefficients  $X_n$  is simply a sum of exponential terms (modes), each of them multiplied by its corresponding complex coefficient  $X_n = a_n + b_n i$ . The total number of coefficients  $N$  was required to be the same for all flow, pressure and volume magnitudes, and it was chosen to be nine (from  $n = 0$  to  $n = 8$ ). This value was sufficiently large to correctly adapt to the original flow data. A lower number of modes failed to accurately represent the flow waveform, while larger  $N$  required longer time to produce the results without really improving them. The vector containing the Fourier coefficients that described a flow signal was ready to be used as input in the model.

### 3. RESULTS AND DISCUSSION

Repeating the same order as in [MATERIALS AND METHODS](#), an evaluation of the model results is presented first, followed by an assessment of the MATLAB script performance at extracting flow data from the MR images (opposite to the actual chronological order). Based on the obtained results, a future line of work to continue with this project will be discussed.

#### 3.1. Model outcomes

This section provides the most relevant observations after comparing the different model variations and tuning the matrix coefficients. Adding complexity to the system did not significantly affect the overall outcome, indicating that certain structures were not crucial for intracranial dynamics. Model C, with a simplified configuration, emerged as the most suitable option to represent the system. Physiological parameters were fitted against experimental MRI measurements, with coefficients related to CSF-filled cavities showing significant impact. However, limitations in available data and potential errors in the measurements should be acknowledged, and the provided parameter values should be viewed as estimations of biological properties.

##### 3.1.1. Results of model comparison

The plots in [FIGURE 3.1](#) were used to visually contrast the results of the different model variations. Since the objective of this comparison was to determine the differences in the general output of each model, the actual amplitude of the signals was not relevant. By looking at the graphs, it becomes clear that adding complexity to the system did not affect the outcome. In fact, when an additional compartment or connection was incorporated into the system, the only visible consequence was that the behavior of variables related to that new structure were simulated while leaving all other signals unchanged.

The meaning behind these results is that the structures represented in the more complex models were not especially important for intracranial dynamics. Going back to the characterization of these structures, we can see that the two passages present in model A (the connection between capillaries and brain, and between brain and cranial SAS) do not represent an open channel, but rather the seepage of fluid through the permeable walls of thin vessels. The resistances of these two passages were defined with six and three orders of magnitude higher than the other resistances, respectively. Therefore, neglecting these connections and assuming a zero flow through them does not significantly alter the overall dynamics of the whole system.

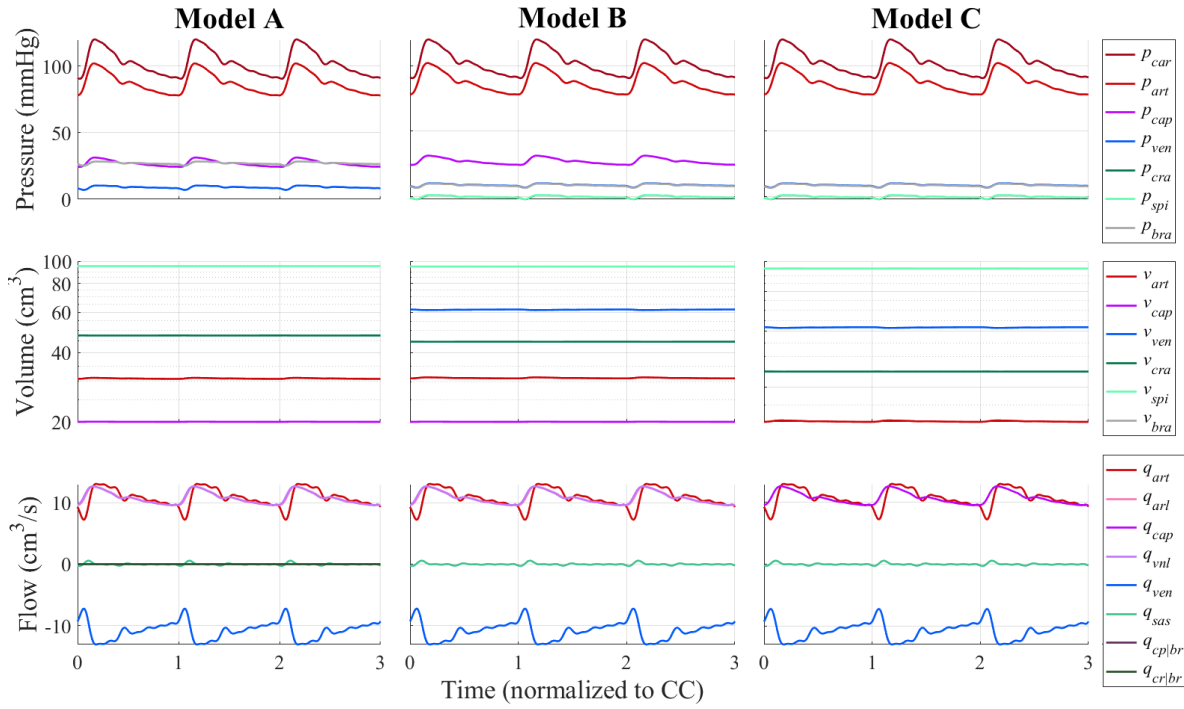


**Figure 3.1. Comparison of models.** The graphs correspond to the output signals of model variations A (left column), B (middle) and C (right). Each subplot contains all signals of a same type of variable: pressure (top), volume (middle) and flow (bottom). A common legend for each type of variable is provided.

On the other hand, the adjustment made between models B and C involved the substitution of the capillary compartment by a vessel directly connecting arteries with veins. This modification constitutes an important simplification because it reduces the number of compartments and equations of the system. The resistance of this new vessel was defined as the sum of the arterioles and venules resistances. Flow and pressure signals corresponding to the old capillary compartment were not plotted in model C, while the signals from all other compartments remained virtually the same. A possible explanation for this minimal impact of the capillary compartment on the overall dynamics is its relatively small size and compliance, compared to the other compartments. These findings suggest that a small structure characterized by minimal changes in volume can be effectively modeled as a connecting vessel, rather than a full compartment.

Therefore, considering that the simplifications on the system did not lead to a poorer or less accurate outcome, model C seemed like the most suitable option to study the dynamics within the skull while maintaining a simple and computationally efficient configuration.

### 3.1.2. Results of coefficient tuning

The different parameters in the system of equations were tuned according to the arterial and CSF flow measured in a subject through MRI. This tuning process signifies an attempt to adapt the model to the real dynamics of the subject, and the final values of the parameters (TABLE 2.3) represent an estimation of the real physiological properties of this individual.

An example of the tuning process is offered in [FIGURE 3.2](#), where the CSF flow signals (experimental from MRI and simulated by model C) are compared to adjust the venous compliance  $C_{ven}$ . Initially, a wide range of order of magnitudes was tested to find the scale of the parameter. A second and third tuning rounds with increasing precision indicated that a value of  $C_{ven} = 0.04 \text{ cm}^3/\text{mmHg}$  would make the model predict the most similar outcome to the experimental data.

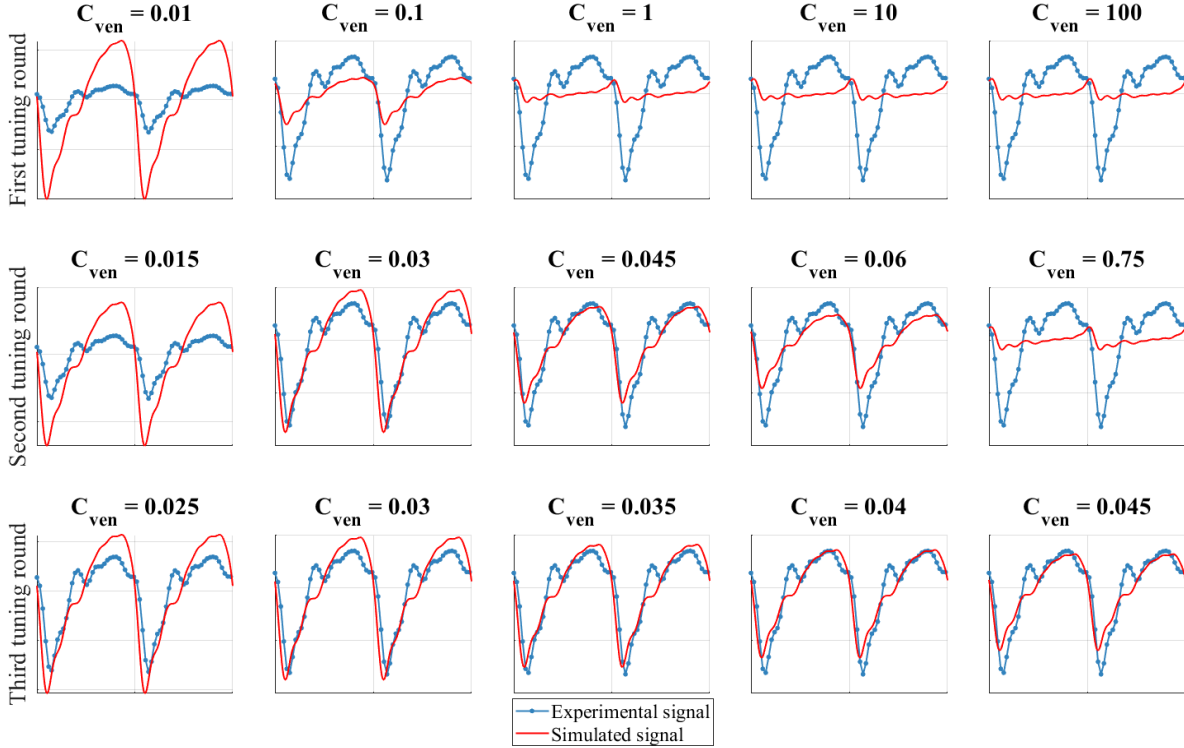


**Figure 3.2. Tuning of venous compliance.** This example shows how the tuning process of parameter  $C_{ven}$  was done by comparing the experimental (blue) and simulated (red) signals of CSF flow in the time domain. In this case, up to three tuning rounds with increasing precision (each of the rows) were realized before setting the final value, which according to the similarity measure (sum of absolute differences) would be  $C_{ven} = 0.04 \text{ cm}^3/\text{mmHg}$ . Experimental data was obtained by MRI and the simulation was performed with model C using measured arterial flow as an input.

Some parameters did not significantly affect (or did not affect at all) the simulation, while others produced very different outcomes, like the example provided above. By looking at [TABLE 2.3](#), one can observe the adjustments made to each parameter. In general, modifications to all volumes at rest did not cause any changes to the simulated CSF flow, suggesting that this magnitude is not especially relevant for fluid dynamics. On the other hand, some resistances did have an important effect on the simulation and were mostly adjusted to higher values, as is the case of  $R_{arl}$ ,  $R_{vnl}$  and  $R_{sas}$ . Finally, compliances showed the highest influence on the system and they were tuned to more precise values. In fact, after modifying all parameters, compliances were further adjusted using the new values just



obtained. The values of  $C_{art}$ ,  $C_{ven}$ ,  $C_{cra}$  and  $C_{spi}$  were tuned at least to the second significant digit.

Interestingly, parameters related to the CSF-filled cavities ( $R_{sas}$ ,  $C_{cra}$  and  $C_{spi}$ ) were among the most determinant and they were all tuned to the third significant digit. This result may be a consequence of using CSF flow as the signal to compare during the tuning process because the just mentioned parameters directly define the mechanic properties of the structures related to this signal (the cranial and spinal cavities, and the resistance of the channel connecting them).

However, it should be mentioned that only the CSF flow —one out of the 14 variables involved in the model— was used in this analysis, and a parameter may have a relevant impact on other variables (flows or pressures). Because experimental data is required to compare with the simulation output, the possibilities to use different variables in the tuning process were limited. Furthermore, experimental CSF flow was considered as a reference criterion and used as the target measure, but this signal came with errors, as it will be discussed in [RESULTS OF FLOW EXTRACTION](#). By adapting the parameters to fit the two signals, these errors would also propagate to the parameters. Therefore, the final values provided in this study for the different physiological properties (resistance and compliance) may not be regarded as proven data but rather as estimations.

## 3.2. Data processing performance

The MATLAB script used to extract flow measures from the MRI data was successful in its task. Results of specific steps in this process are presented here together with illustrations produced by the code. The distortion caused by velocity encoding constraints was eliminated and the effectiveness of the Fourier transformation was demonstrated. Additionally, the consistency exhibited by blood and CSF flow signals obtained by the algorithm is discussed.

### 3.2.1. Results of aliasing removal

The aliasing distortion caused by the constraints of the velocity encoding was successfully removed with the algorithm developed for such end. [FIGURE 3.3](#) offers a visual depiction of how measurements with different VENC yielded different flow outputs (notice that the figure displays the evolution of flows through the vessel, not velocities). Flow values for the lowest VENC (lightest blue line) are closer to 0 because the measurable velocity range was bounded to  $\pm 10$  cm/s, while using a higher VENC (darker blue) offered a wider range able to encompass higher velocities (and therefore flows). It can be observed that the corrected flow (red line) generally adapts to the shape of the maximum VENC, which indicates that the algorithm effectively adjusted the flow measurements. The *VEN RIJV* subplot provides a good example: flow values for all VENC during the first milliseconds coincide but, at some point, the real velocity exceeds the negative boundary of  $-10$  cm/s and the line for this series no longer follows the same path as the other two series. However, the algorithm was able to



detect this change and adapt the values of the lowest VENC to align them with the higher VENC.

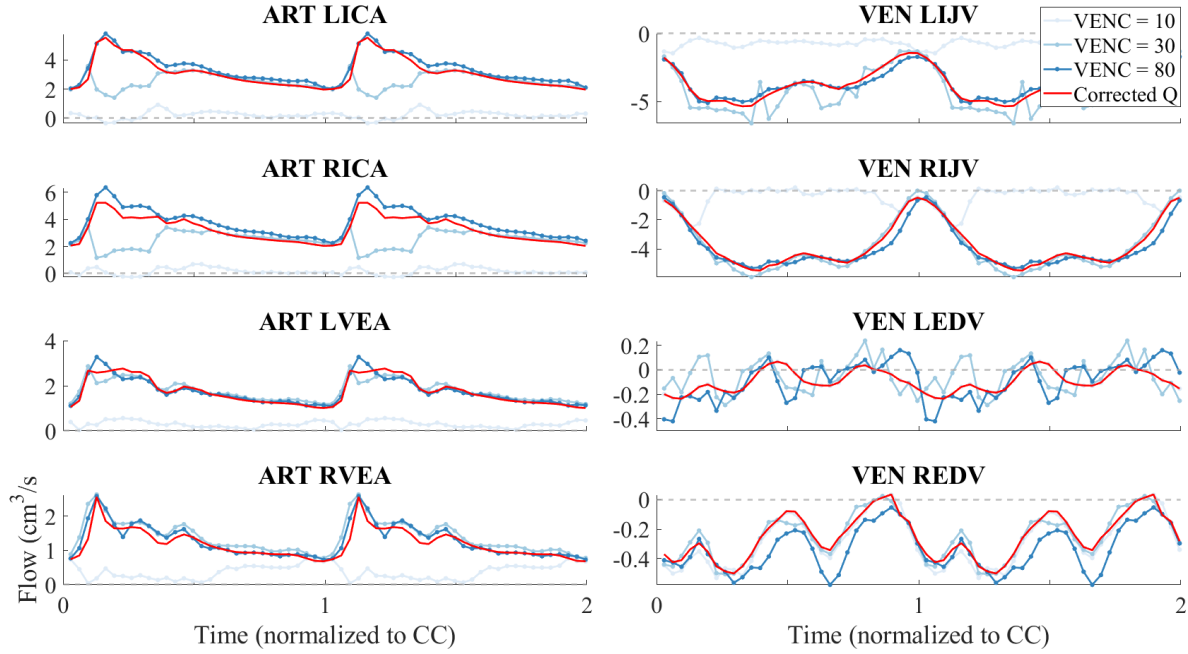


**Figure 3.3. Blood flow through each vessel along the cardiac cycle.** Each diagram shows the flow of a different arterial (ART) or venous (VEN) vessel for the different velocity encodings (10, 30 and 80 cm/s in different shades of blue) and the computed flow after removing aliasing (red). The signals have been repeated in time for easier visualization. LICA/RICA = left/right internal carotid artery. LVEA/RVEA = left/right vertebral artery. LIJV/RIJV = left/right internal jugular vein. LEDV/REDV = left/right epidural vein.

### 3.2.2. Results of flow extraction

On the other hand, [FIGURE 3.4](#) depicts the total flow through arterial, venous and CSF regions. These total flows result from the sum of individual flow signals through each respective vessel. Arterial flow consistently maintains a positive value, ranging between 5 and 15  $\text{cm}^3/\text{s}$ , which indicates a permanent inflow of blood into the cranial cavity. On the contrary, venous flow exhibits only negative values as expected from a continuous outflow. The average cerebral blood flow was found to be 9.36  $\text{cm}^3/\text{s}$ , a number that lies close enough to other published measurements (11.95  $\text{cm}^3/\text{s}$ ) [43]. Maximum peaks on arterial and venous signals occur simultaneously, which are caused by the systolic pressure peak of the CC. Notably, the pulsatility in arterial flow is more abrupt than in the veins due to the proximity of arteries to the heart.

CSF displays an oscillatory motion around zero, a consequence of the arterial pulsatility being transferred to the internal cavities of the brain and eventually to the CSF, causing it to oscillate between the cranial and spinal compartments. This oscillation is a response to the arterial peak inflow, which forces CSF to exit the cranium according to the Monro–Kellie doctrine. The net CSF flow estimated from the MRI data was 0.377  $\text{cm}^3$  positive per CC. Assuming an enclosed spinal cavity where CSF is neither produced nor absorbed, the net

flow through the foramen magnum should be minimal or zero, as other research studies have obtained [44]. While the value obtained in this study was not zero, it falls relatively close to it. The accumulation of errors from MRI noise, ROI selection, non-removed aliasing or a low temporal resolution may be the cause of the small offset.

All these fluid dynamics are consistent with the current theories, models and measurements of blood and CSF pulsatility, meaning that flow extraction from MR images was successful and that the signals obtained represent the real dynamics with accuracy.

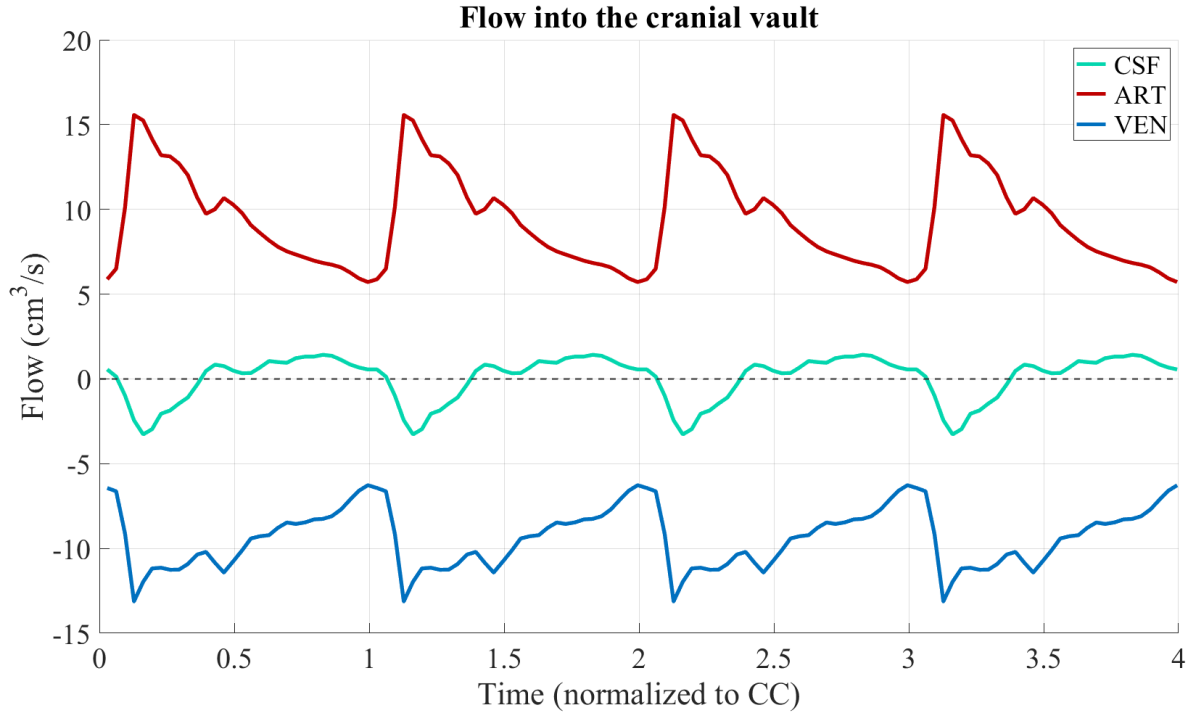


**Figure 3.4. Flow in and out of the cranial cavity.** Arterial (red), venous (blue) and CSF (turquoise) flows are plotted along four cardiac cycles. These signals contain the thirty flow data points obtained from MR images. Positive values represent cephalic flow (entering the skull) and negative values indicate flow in the caudal direction (exiting the skull).

### 3.2.3. Results of Fourier transformation

A comparison between the MRI-derived data and its reconstruction from Fourier coefficients is also given in [FIGURE 3.5](#) in order to check the accuracy of this transformation. The reconstructed signals perfectly adapt to the original data points, which proves that the set of nine complex Fourier coefficients correctly describes the behavior of the signal and can be used to represent it with precision and accuracy. Furthermore, using the coefficients to express the signal implies a reduction in data amount since only nine coefficients were used compared to the thirty original data measurements, and it allows to obtain a signal that is continuous in time, rather than a discrete set of points. Hence, the technique of using Fourier coefficients yielded a more compact representation of the flows with a higher temporal precision.

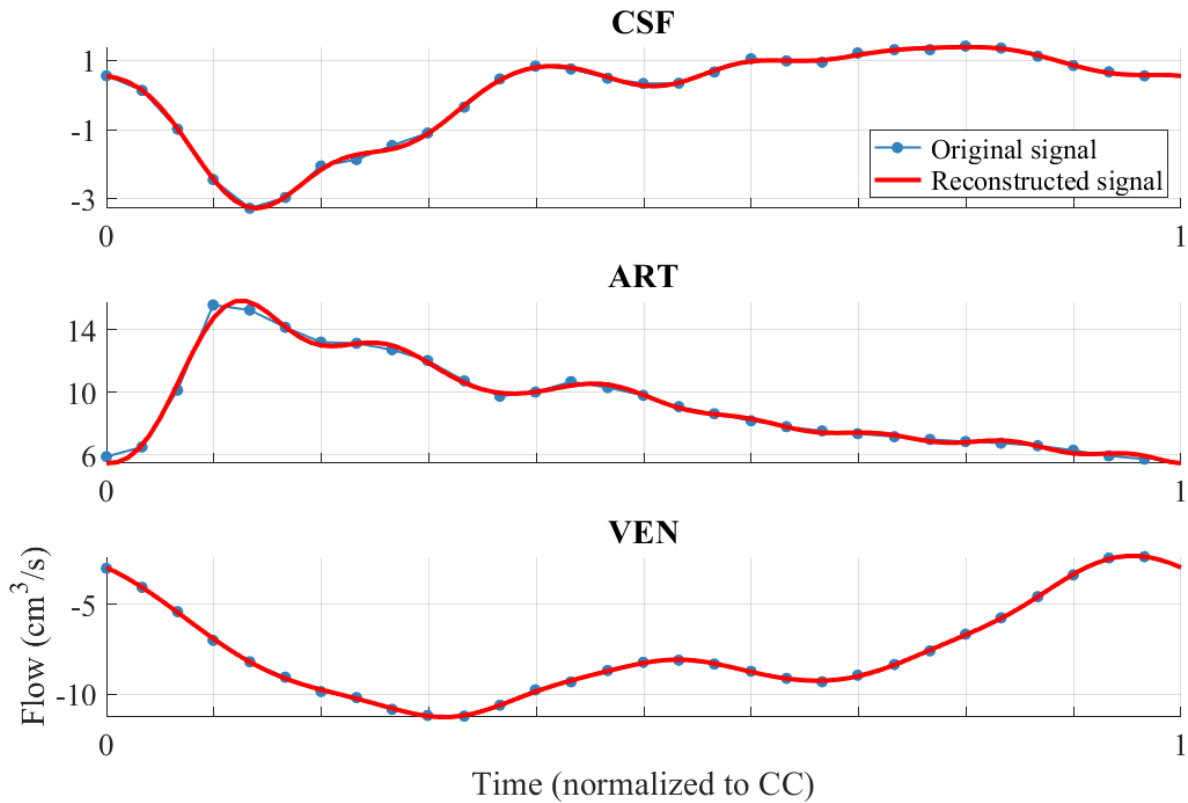


**Figure 3.5. Comparison of original and reconstructed flow signals.** Both the original data points (blue) and the signal reconstructed from the Fourier coefficients (red) are plotted for each region. The reconstructed signal was plotted with a higher temporal resolution (100 data points).

### 3.3. Final review

The possibilities of the model and the pre-processing MATLAB code are discussed in a final assessment. Similarly, some limitations or difficulties encountered during the project will be reviewed, along with suggestions on how to overcome them in future research.

#### 3.3.1. Results evaluation

Results yielded by the analysis of resistance and compliance parameters are in line with clinical measures and outcomes from other research studies. Except for the resistance in venules and cranial-spinal SAS channel, the majority of obtained values fall within the range or order of magnitude of the literature references that were used as a starting point (see [TABLE 2.3](#) to compare). A model returning such positive results seems to be promising and with potential to help in the investigation of intracranial pulsatility. However, the lack of a bigger data set and additional subjects (healthy and pathological) means that the results obtained here may not faithfully represent the performance and effectiveness of the model proposed, and any conclusions should be promulgated with caution.

On a separate note, the successful performance of the algorithm to remove velocity aliasing allowed this project to take advantage of the full possibilities of MRI by combining the

precision of a low VENC with the wide range of a high VENC. Several phase-unwrapping techniques have been used across the scientific community to remove this aliasing artifact in MRI, from detecting and fixing discontinuities on temporal and spatial velocity values [45] [46] to deep learning methods such as convolutional neural networks [41]. The solution presented in this thesis is yet another tool in a wide range of options that researchers can consider when addressing this issue. While our method required the acquisition of three MRI series with different VENC, the proposed technique is fast, efficient and easy to implement on MATLAB and other programming languages.

Similarly, the approach used to represent a signal as a set of complex Fourier coefficients proved to be accurate, as already explained. While this course of action may seem like a mere choice of mathematical representation, the possibilities it entails have very useful applications. As mentioned before, the signal could be compacted into a short vector of complex coefficients that requires less storage than the original data points but still contains all the information needed to reconstruct the signal in the time domain. In code, this representation is practical for the application of any further transformation or processing of the signal. On top of that, this work has demonstrated how a continuous signal can be faithfully reconstructed from this set of coefficients, which enables a study of the signal with high temporal resolution. This forward and backward transformation of the signal from temporal to frequency domain is fast and easy to implement in a MATLAB script or using any other programming language.

### **3.3.2. Limitations and future outlook**

One of the objectives defined in the introduction of this thesis was to test the model with patient images in an effort to obtain indicators of pathologies from the model simulations. However, the opportunity of accessing MRI data from subjects of interest (patients with hydrocephalus or syringomyelia) did not present itself. Due to the legal protection of privacy and strong regulation on medical data, access to suitable MR images was not possible. Therefore, additional validation of the model with a clinical dataset remains as a future objective.

On the other hand, the process of manually calibrating the matrix coefficients to derive accurate estimates of resistance and compliance parameters was laborious, time-consuming and inefficient due to the large number of dimensions. However, this process could easily be streamlined and automated through the implementation of an optimization algorithm. By defining a cost function that quantifies the dissimilarity between experimental and simulated signal, the task could be addressed as a minimization problem. The set of parameters involved in the equations would define a multidimensional space where the global minimum of the cost function should be found. Moreover, a properly designed cost function could directly compare the signals as Fourier coefficients, eliminating the need for converting them to temporal domain. Genetic algorithms and particle swarm optimization are suitable candidates

with the potential to solve global optimizations problems in multidimensional spaces, like the one presented here.

Regarding the processing of MR images, regions of interest were manually defined by selecting the perimeter of vessels on-screen in one of the time frames of each series. This task is time-consuming and requires the help of an expert on interpreting MRI images. Besides, tissue motion between time frames will negatively affect the accuracy of the selection. An automated approach was considered as a possible alternative to this methodology. A paper was found that used a frequency-based technique to automatically find pixels where the temporal variations followed the fundamental frequency of the CC [47]. These pixels would correspond to regions where pulsatility coupled to the heartbeat was strong, effectively finding the ROIs associated with the relevant vessels. This approach was not implemented in the code due to time restrictions, but it remains an interesting course of action to make the process of ROI selection easier, faster and more accurate.

On a different note, new studies suggest that the effect of respiration on CSF flow could be greater than that one of the cardiac component [48]. If this new hypothesis is correct, respiration should not be neglected in the model. It would be interesting to adjust the model design so as to accommodate a new breathing component and investigate its effect on CSF pulsatility.

## 4. REGULATORY FRAMEWORK

This project was conducted following all the necessary legal, ethical and safety requirements, in accordance with local and national regulations. Technical standards on code production and thesis elaboration were considered. Information about the intellectual property regarding the project and thesis report is also provided.

### 4.1. Legislation analysis

Clinical data in Spain and the European Union is considered private and personal to the patient, and its protection is regarded as a fundamental right. Thus, there is a rigorous legal framework to ensure that individuals maintain control over their personal health information, while the publication and use of this type of data is strictly protected under the Spanish law *Ley de autonomía del paciente*<sup>1</sup>, which stipulates the following:

*“Toda persona tiene derecho a que se respete el carácter confidencial de los datos referentes a su salud, y a que nadie pueda acceder a ellos sin previa autorización amparada por la Ley.”*

“Every person has the right to have the confidential nature of their health data respected, and that no one can access them without prior authorization protected by the Law.”

Artículo 7 de la Ley 41/2002 de 14 de noviembre [49].

This Law aligns with international conventions and regulations, such as the Declaration of Helsinki by the World Medical Association (Paragraph 24) [50] that emphasizes the importance of privacy protection for research subjects, and the General Data Protection Regulation of the European Union (Article 9) [51], which recognizes health data as a special category of personal data that requires enhanced protection. Consequently, the use of any medical images for educational or research purposes, including those used in this thesis, must be granted explicit consent by the patient for such purposes. Additionally, if permission is granted for the employment of clinical data, appropriate anonymization must be applied to the data in order to ensure the patient’s information remains undisclosed, and the patient unidentified.

With these restrictions in place, the utilization of original patient images in this project was not possible. However, MR images from a healthy individual were used to extract real flow data and build the model. These images were voluntarily provided with complete knowledge about the motivation and intentions of the research being conducted. A consent form was filled in and signed before acquisition to ensure that ethical considerations and legal requirements were met.

---

<sup>1</sup> “Law of autonomy of the patient”

On a different side, software licenses were required for some of the programs and tools used in this project. Access to the MATLAB platform was made possible through the Campus-Wide License offered by University Carlos III of Madrid, which provides unlimited usage of MATLAB and Simulink to all University students and faculty members. The thesis report was written using Microsoft Word as part of the Office 365 Education license, also granted by UC3M.

## **4.2. Technical standards**

The MATLAB scripts employed to build the model are original and were developed considering code organization, readability and clarity. Different steps in the process of initializing and running the model are identified by titles, organizing the script into blocks for a clearer comprehension of the workflow. Comments were incorporated to explain the purpose and functionality of the code, and to help the user in its understanding.

This report was written following the recommendations proposed by UC3M for structure, format and style of a bachelor's thesis on an engineering subject, and the IEEE guidelines for in-text citation and references. The majority of articles, books and other sources cited throughout the report are open access, with a small portion of them being accessed with the login credentials of a UC3M student account. An attempt was made to find recent peer-reviewed articles published in reputable and impactful scientific journals. Special attention was dedicated to providing original research work and to avoiding the presence of plagiarism.

## **4.3. Intellectual property**

As it is indicated in the cover page, this work is licensed under Creative Commons CC BY-NC-ND 4.0 (Attribution – Non-Commercial – No Derivatives), which means that it can be accessed, cited and distributed in any format as long as the user gives the corresponding attribution to the author, does not use the work for commercial purposes and does not modify the material. The methodology and the model proposed here can be freely replicated by other researchers that may be interested in doing so, as it is not restricted by any patent or other intellectual property rights. Access to the original code scripts can be granted upon request to the thesis author through the following email: [josu.ps13@gmail.com](mailto:josu.ps13@gmail.com).

## 5. SOCIO-ECONOMIC ENVIRONMENT

An estimated breakdown of the costs of this project and its social impact on the biomedical industry are provided in this section.

### 5.1. Project budget

This project required very little specialized machinery or informatic software. [TABLE 5.1](#) summarizes the devices and programs that were somehow involved in the thesis development, as well as the regular price of the products and licenses. Human resources collaborating in the investigation are also included. However, it should be mentioned that the real cost of this research work is unknown, since some programs were obtained under special licenses provided by UC3M whose prices are not publicly available.

**Table 5.1. Breakdown of the project budget.** Total costs are divided into three categories: *hardware*, *software* and *human resources*. The type of license for the programs is specified and personnel are identified by their role in the project and their position at University Carlos III of Madrid.

Category	Product/Personnel	Item	Price
Hardware	<b>MRI acquisition</b> Siemens MAGNETOM Prisma Fit 3T	Price of 2-hour session <sup>1</sup> :	1,000.00€
Software	<b>MATLAB</b> Academic license	Annual price <sup>2</sup> :	262.00€
	<b>Microsoft 365</b> Microsoft 365 Personal	Annual price <sup>3</sup> :	69.00€
Human resources	<b>Thesis author</b> Undergraduate student at UC3M, part-time internship (22.5 h/week)	Salary <sup>4</sup> (1,231.79 €/month × 4 months):	4,927.16€
		Social Security (32.6%):	1,606.25€
		Total price of internship:	6,533.41€
Total cost			7,864.41€

### 5.2. Social impact

The model developed during this project is expected to have a relevant impact on healthcare regarding the understanding and diagnosis of CSF-related disorders such as syringomyelia and hydrocephalus. As it was explained in the [MOTIVATION](#), a sound approach to address these neurological diseases is to foster their early diagnosis. The compartmental model has the potential to fulfill this objective by providing a reliable, non-invasive tool for identifying abnormalities in the CSF dynamics, which can serve as a valuable decision-support resource

<sup>1</sup> Prices available on *Centro de Investigación Científica* official webpage <https://cic.ugr.es>.

<sup>2</sup> Prices available on MATLAB official webpage <https://www.mathworks.com>.

<sup>3</sup> Prices available on Microsoft official webpage <https://www.microsoft.com>.

<sup>4</sup> Prices available in the salary table of UC3M.



for clinicians, facilitating early detection of these conditions and ultimately improving patient's quality of life.

In addition, the implementation of the algorithm is fast, cost-effective and can be used to study a range of different conditions affecting CSF pulsatility. Moreover, it offers an interesting opportunity to investigate some of the target conditions that do not receive much attention and research due to their low prevalence among the population, such as syringomyelia which is considered a rare disease. Other medical problems, like hydrocephalus, are more common and extensively studied. However, valuable insights into the underlying mechanisms of their pathophysiology can still be derived from simulation models like this one, and treatment effectiveness can also be evaluated in this context.

## 6. CONCLUSION

After tuning the physiological parameters involved in the equations, the simulation of CSF flow provided by the model adjusted quite accurately to the experimental signal. This means that the model can successfully replicate fluid dynamics and that it represents a computational tool useful in the investigation of intracranial pulsatility. Moreover, the developed model follows the compartmental approach, indicating that its implementation is fast and computationally efficient, avoiding the need for powerful computers.

The developed MATLAB script demonstrated to be successful in extracting flow data from MR images. Aliasing distortions were effectively corrected and the resulting blood and CSF flow signals were consistent with expected physiological dynamics, which indicates that the selection of vessels of interest and the computation of flow variables was correct. On top of that, the Fourier transformation technique proved accurate in representing the flow signals, allowing for a more compact representation and higher temporal precision.

However, some limitations and challenges were identified in the project, mainly relating to the lack of automation of certain processes such as the calibration of matrix or the selection of regions of interest. The exploration of alternatives to streamline these tasks remains appealing as it would improve accuracy and efficiency and relieve the user of time-consuming procedures. Besides, the model could only be tested with data from one individual, which is not enough to provide confident results. Future research could benefit from expanding the data set, including healthy and pathological subjects, to better assess the model's performance and effectiveness.

In summary, the results produced during this project seem promising for the investigation of CSF pulsatility, which fulfills the main purpose and motivation of the thesis. The simulations conducted by the model adjusted adequately to experimental measurements and the performance of the script to process MR images was satisfactory. Nonetheless, there is room for further enhancements in the methodology, and the implementation of the model on pathological subjects remains a necessary task to study abnormal conditions.

## BIBLIOGRAPHY

- [1] J. E. Hall and M. E. Hall, *Guyton and Hall Textbook of Medical Physiology*, 11th ed. Elsevier Health Sciences, 2020.
- [2] OpenStax, *CSF Circulation*. 2016. Accessed: May 17, 2023. [Online]. Available: [https://commons.wikimedia.org/wiki/File:1317\\_CFS\\_Circulation.jpg](https://commons.wikimedia.org/wiki/File:1317_CFS_Circulation.jpg)
- [3] R. Spector, S. Robert Snodgrass, and C. E. Johanson, “A balanced view of the cerebrospinal fluid composition and functions: Focus on adult humans,” *Exp. Neurol.*, vol. 273, pp. 57–68, Nov. 2015, doi: 10.1016/j.expneurol.2015.07.027.
- [4] M. Nedergaard, “Garbage truck of the brain,” *Science*, vol. 340, no. 6140, pp. 1529–1530, Jun. 2013, doi: 10.1126/science.1240514.
- [5] A. A. Linninger, K. Tangen, C.-Y. Hsu, and D. Frim, “Cerebrospinal Fluid Mechanics and Its Coupling to Cerebrovascular Dynamics,” *Annu. Rev. Fluid Mech.*, vol. 48, no. 1, pp. 219–257, 2016, doi: 10.1146/annurev-fluid-122414-034321.
- [6] F. jpg: C. N. at E. Wikipedia, *Syringomyelia (with arrow)*. 2020. Accessed: May 18, 2023. [Online]. Available: [https://commons.wikimedia.org/wiki/File:Syringomyelia\\_\(with\\_arrow\).png](https://commons.wikimedia.org/wiki/File:Syringomyelia_(with_arrow).png)
- [7] MBq, *MBq Hydrocephalus*. 2005. Accessed: May 18, 2023. [Online]. Available: [https://commons.wikimedia.org/wiki/File:MBq\\_Hydrocephalus.jpg](https://commons.wikimedia.org/wiki/File:MBq_Hydrocephalus.jpg)
- [8] “Hydrocephalus,” *National Institute of Neurological Disorders and Stroke*. <https://www.ninds.nih.gov/health-information/disorders/hydrocephalus> (accessed May 16, 2023).
- [9] “Syringomyelia,” *National Institute of Neurological Disorders and Stroke*. <https://www.ninds.nih.gov/health-information/disorders/syringomyelia> (accessed May 17, 2023).
- [10] A. M. Isaacs *et al.*, “Age-specific global epidemiology of hydrocephalus: Systematic review, metanalysis and global birth surveillance,” *PLoS ONE*, vol. 13, no. 10, p. e0204926, Oct. 2018, doi: 10.1371/journal.pone.0204926.
- [11] “Syringomyelia: Background, Pathophysiology, Etiology,” Apr. 2023, Accessed: May 16, 2023. [Online]. Available: <https://emedicine.medscape.com/article/1151685-overview>
- [12] L. Miah *et al.*, “Incidence, Prevalence, and Health Care Outcomes in Idiopathic Intracranial Hypertension: A Population Study,” *Neurology*, vol. 96, no. 8, pp. e1251–e1261, Feb. 2021, doi: 10.1212/WNL.00000000000011463.
- [13] A. F. Struck and V. M. Haughton, “Idiopathic Syringomyelia: Phase-Contrast MR of Cerebrospinal Fluid Flow Dynamics at Level of Foramen Magnum,” *Radiology*, vol. 253, no. 1, pp. 184–190, Oct. 2009, doi: 10.1148/radiol.2531082135.
- [14] S. Qvarlander *et al.*, “Cerebrospinal fluid and blood flow patterns in idiopathic normal pressure hydrocephalus,” *Acta Neurol. Scand.*, vol. 135, no. 5, pp. 576–584, May 2017, doi: 10.1111/ane.12636.

- [15] V. Kurtcuoglu, K. Jain, and B. A. Martin, “Modelling of Cerebrospinal Fluid Flow by Computational Fluid Dynamics,” in *Biomechanics of the Brain*, K. Miller, Ed., in Biological and Medical Physics, Biomedical Engineering. Cham: Springer International Publishing, 2019, pp. 215–241. doi: 10.1007/978-3-030-04996-6\_9.
- [16] M. Gresch, R. Brügger, A. Meyer, and W. Gujer, “Compartmental Models for Continuous Flow Reactors Derived from CFD Simulations,” *Environ. Sci. Technol.*, vol. 43, no. 7, pp. 2381–2387, Apr. 2009, doi: 10.1021/es801651j.
- [17] “PubMed,” *PubMed*. <https://pubmed.ncbi.nlm.nih.gov/> (accessed Jun. 03, 2023).
- [18] “Scopus.” <https://www.scopus.com/search/form.uri#basic> (accessed Jun. 03, 2023).
- [19] “Observations on the Structure and Functions of the Nervous System, Illustrated with Tables,” *Lond. Med. J.*, vol. 4, no. 2, pp. 113–135, 1783.
- [20] S. Sorek, J. Bear, and Z. Karni, “Resistances and compliances of a compartmental model of the cerebrovascular system,” *Ann. Biomed. Eng.*, vol. 17, no. 1, pp. 1–12, Jan. 1989, doi: 10.1007/BF02364270.
- [21] B. Cohen, A. Voorhees, S. Vedel, and T. Wei, “Development of a theoretical framework for analyzing cerebrospinal fluid dynamics,” *Cerebrospinal Fluid Res.*, vol. 6, no. 1, p. 12, Sep. 2009, doi: 10.1186/1743-8454-6-12.
- [22] A. A. Linninger *et al.*, “Pulsatile cerebrospinal fluid dynamics in the human brain,” *IEEE Trans. Biomed. Eng.*, vol. 52, no. 4, pp. 557–565, Apr. 2005, doi: 10.1109/TBME.2005.844021.
- [23] A. A. Linninger, M. Xenos, B. Sweetman, S. Ponkshe, X. Guo, and R. Penn, “A mathematical model of blood, cerebrospinal fluid and brain dynamics,” *J. Math. Biol.*, vol. 59, no. 6, pp. 729–759, Dec. 2009, doi: 10.1007/s00285-009-0250-2.
- [24] M. Causemann, V. Vinje, and M. E. Rognes, “Human intracranial pulsatility during the cardiac cycle: a computational modelling framework,” *Fluids Barriers CNS*, vol. 19, no. 1, p. 84, Nov. 2022, doi: 10.1186/s12987-022-00376-2.
- [25] M. Galarza and J. A. Lazareff, “Transcranial Doppler in infantile cerebrospinal fluid disorders: clinical validity,” *Neurol. Res.*, vol. 26, no. 4, pp. 409–413, Jun. 2004, doi: 10.1179/016164104225016010.
- [26] B. L. C. Wright, J. T. F. Lai, and A. J. Sinclair, “Cerebrospinal fluid and lumbar puncture: a practical review,” *J. Neurol.*, vol. 259, no. 8, pp. 1530–1545, Aug. 2012, doi: 10.1007/s00415-012-6413-x.
- [27] S. Munakomi and J. M Das, “Intracranial Pressure Monitoring,” in *StatPearls*, Treasure Island (FL): StatPearls Publishing, 2023. Accessed: Jun. 04, 2023. [Online]. Available: <http://www.ncbi.nlm.nih.gov/books/NBK542298/>
- [28] A. Abdrabou, “Acute disseminated encephalomyelitis | Radiology Case | Radiopaedia.org,” *Radiopaedia*. <https://radiopaedia.org/cases/acute-disseminated-encephalomyelitis-4> (accessed May 31, 2023).
- [29] N. H. Mehta *et al.*, “Quantifying cerebrospinal fluid dynamics: A review of human neuroimaging contributions to CSF physiology and neurodegenerative disease,” *Neurobiol. Dis.*, vol. 170, p. 105776, Aug. 2022, doi: 10.1016/j.nbd.2022.105776.

- [30] K. M. Saqr *et al.*, “Physiologic blood flow is turbulent,” *Sci. Rep.*, vol. 10, no. 1, Art. no. 1, Sep. 2020, doi: 10.1038/s41598-020-72309-8.
- [31] B. Mokri, “The Monro–Kellie hypothesis: Applications in CSF volume depletion,” *Neurology*, vol. 56, no. 12, pp. 1746–1748, Jun. 2001, doi: 10.1212/WNL.56.12.1746.
- [32] M. Di Rienzo, A. Avolio, G. Rizzo, Z. M. I. Zeybek, and L. Cucugliato, “Multi-Site Pulse Transit Times, Beat-to-Beat Blood Pressure, and Isovolumic Contraction Time at Rest and Under Stressors,” *IEEE J. Biomed. Health Inform.*, vol. 26, no. 2, pp. 561–571, Feb. 2022, doi: 10.1109/JBHI.2021.3101976.
- [33] V. Vinje *et al.*, “Respiratory influence on cerebrospinal fluid flow – a computational study based on long-term intracranial pressure measurements,” *Sci. Rep.*, vol. 9, no. 1, Art. no. 1, Jul. 2019, doi: 10.1038/s41598-019-46055-5.
- [34] A. Avolio, B. Spronck, I. Tan, J. Cox, and M. Butlin, “Chapter 1 - Basic principles that determine relationships between pulsatile hemodynamic phenomena and function of elastic vessels,” in *Textbook of Arterial Stiffness and Pulsatile Hemodynamics in Health and Disease*, J. A. Chirinos, Ed., Academic Press, 2022, pp. 3–26. doi: 10.1016/B978-0-323-91391-1.00001-7.
- [35] Y. Zhang, S. F. Sia, M. K. Morgan, and Y. Qian, “Flow resistance analysis of extracranial-to-intracranial (EC–IC) vein bypass,” *J. Biomech.*, vol. 45, no. 8, pp. 1400–1405, May 2012, doi: 10.1016/j.jbiomech.2012.02.025.
- [36] K.-H. Støverud, H. P. Langtangen, G. A. Ringstad, P. K. Eide, and K.-A. Mardal, “Computational Investigation of Cerebrospinal Fluid Dynamics in the Posterior Cranial Fossa and Cervical Subarachnoid Space in Patients with Chiari I Malformation,” *PLoS ONE*, vol. 11, no. 10, p. e0162938, Oct. 2016, doi: 10.1371/journal.pone.0162938.
- [37] “Phase-Contrast MRI: Physics, Techniques, and Clinical Applications.” <https://pubs.rsna.org/doi/epdf/10.1148/rg.2020190039> (accessed May 02, 2023).
- [38] NEMA PS3 / ISO 12052, Digital Imaging and Communications in Medicine (DICOM) Standard. Rosslyn, VA, USA. Available: <http://medical.nema.org/>
- [39] W. D. Bidgood, S. C. Horii, F. W. Prior, and D. E. Van Syckle, “Understanding and Using DICOM, the Data Interchange Standard for Biomedical Imaging,” *J. Am. Med. Inform. Assoc.*, vol. 4, no. 3, pp. 199–212, 1997.
- [40] J. Lotz, C. Meier, A. Leppert, and M. Galanski, “Cardiovascular flow measurement with phase-contrast MR imaging: basic facts and implementation,” *Radiogr. Rev. Publ. Radiol. Soc. N. Am. Inc.*, vol. 22, no. 3, pp. 651–671, 2002, doi: 10.1148/radiographics.22.3.g02ma11651.
- [41] H. Berhane *et al.*, “Deep learning–based velocity antialiasing of 4D-flow MRI,” *Magn. Reson. Med.*, vol. 88, no. 1, pp. 449–463, 2022, doi: 10.1002/mrm.29205.
- [42] L. E. Ma, M. Markl, K. Chow, A. Vali, C. Wu, and S. Schnell, “Efficient triple-VENC phase-contrast MRI for improved velocity dynamic range,” *Magn. Reson. Med.*, vol. 83, no. 2, pp. 505–520, Feb. 2020, doi: 10.1002/mrm.27943.
- [43] L. Zarrinkoob, K. Ambarki, A. Wåhlin, R. Birgander, A. Eklund, and J. Malm, “Blood flow distribution in cerebral arteries,” *J. Cereb. Blood Flow Metab. Off. J. Int. Soc.*

- Cereb. Blood Flow Metab.*, vol. 35, no. 4, pp. 648–654, Mar. 2015, doi: 10.1038/jcbfm.2014.241.
- [44] B. J. Iskandar, M. Quigley, and V. M. Haughton, “Foramen magnum cerebrospinal fluid flow characteristics in children with Chiari I malformation before and after craniocervical decompression,” *J. Neurosurg. Pediatr.*, vol. 101, no. 2, pp. 169–178, Nov. 2004, doi: 10.3171/ped.2004.101.2.0169.
- [45] M. Untenberger *et al.*, “Spatiotemporal phase unwrapping for real-time phase-contrast flow MRI,” *Magn. Reson. Med.*, vol. 74, no. 4, pp. 964–970, 2015, doi: 10.1002/mrm.25471.
- [46] M. F. Salfity, J. M. Huntley, M. J. Graves, O. Marklund, R. Cusack, and D. A. Beauregard, “Extending the dynamic range of phase contrast magnetic resonance velocity imaging using advanced higher-dimensional phase unwrapping algorithms,” *J. R. Soc. Interface*, vol. 3, no. 8, pp. 415–427, Jun. 2006, doi: 10.1098/rsif.2005.0096.
- [47] O. Balédent, M. C. Henry-Feugeas, and I. Idy-Peretti, “Cerebrospinal fluid dynamics and relation with blood flow: a magnetic resonance study with semiautomated cerebrospinal fluid segmentation,” *Invest. Radiol.*, vol. 36, no. 7, pp. 368–377, Jul. 2001, doi: 10.1097/00004424-200107000-00003.
- [48] A. Delaidelli and A. Moiraghi, “Respiration: A New Mechanism for CSF Circulation?,” *J. Neurosci.*, vol. 37, no. 30, pp. 7076–7078, Jul. 2017, doi: 10.1523/JNEUROSCI.1155-17.2017.
- [49] Jefatura del Estado, *Ley 41/2002, de 14 de noviembre, básica reguladora de la autonomía del paciente y de derechos y obligaciones en materia de información y documentación clínica*, vol. BOE-A-2002-22188. 2002, pp. 40126–40132. Accessed: May 19, 2023. [Online]. Available: <https://www.boe.es/eli/es/l/2002/11/14/41>
- [50] World Medical Association, “World Medical Association Declaration of Helsinki: Ethical Principles for Medical Research Involving Human Subjects,” *JAMA*, vol. 310, no. 20, pp. 2191–2194, Nov. 2013, doi: 10.1001/jama.2013.281053.
- [51] *Regulation (EU) 2016/679 of the European Parliament and of the Council of 27 April 2016 on the protection of natural persons with regard to the processing of personal data and on the free movement of such data, and repealing Directive 95/46/EC (General Data Protection Regulation) (Text with EEA relevance)*. 2016. Accessed: May 19, 2023. [Online]. Available: <http://data.europa.eu/eli/reg/2016/679/2016-05-04/eng>

## ANNEX

The systems of equations used for model variations A and B in [FIGURE 2.3](#) are provided in this annex. The meaning of each variable can be read in [TABLE 2.1](#). Model A was the original and more complete configuration. All six compartments are included, as well as the flows between capillaries and brain, and between brain and cranial SAS. The system of equations ([Eq. A.1](#)) contains 19 equations and 18 unknowns.

$$\left\{ \begin{array}{lll}
 \text{Pressure drop} & \text{Compartment distension} & \text{Flow continuity} \\
 p_{car} - p_{art} = R_{art} q_{art} & p_{art} - p_{bra} = \frac{v_{art} - V_{o,art}}{C_{art}} & \frac{dv_{art}}{dt} = q_{art} - q_{arl} \\
 p_{art} - p_{cap} = R_{arl} q_{arl} & p_{cap} - p_{bra} = \frac{v_{cap} - V_{o,cap}}{C_{cap}} & \frac{dv_{cap}}{dt} = q_{arl} - q_{vnl} - q_{cp|br} \\
 p_{cap} - p_{ven} = R_{vnl} q_{vnl} & p_{ven} - p_{bra} = \frac{v_{ven} - V_{o,ven}}{C_{ven}} & \frac{dv_{ven}}{dt} = q_{ven} + q_{vnl} \\
 p_{jug} - p_{ven} = R_{ven} q_{ven} & p_{cra} - p_{bra} = \frac{v_{cra} - V_{o,cra}}{C_{cra}} & \frac{dv_{cra}}{dt} = q_{sas} - q_{cr|br} \\
 p_{spi} - p_{cra} = R_{sas} q_{sas} & p_{spi} - P_{out} = \frac{v_{spi} - V_{o,spi}}{C_{spi}} & \frac{dv_{spi}}{dt} = -q_{sas} \\
 p_{cap} - p_{bra} = R_{cp|br} q_{cp|br} & & \frac{dv_{bra}}{dt} = q_{cp|br} + q_{cr|br} \\
 p_{cra} - p_{bra} = R_{cr|br} q_{cr|br} & & \\
 \text{Monro-Kellie doctrine} & & \\
 v_{art} + v_{cap} + v_{ven} + v_{cra} + v_{bra} = V_{tot} & & 
 \end{array} \right.$$

(A.1)

On the other hand, variation B is based on model A with some minor adjustments: fluid transfer from capillaries to the brain, as well as between the brain and the cranial SAS are neglected. Therefore, brain volume is maintained constant. The corresponding system ([Eq. A.2](#)) is composed of 16 equations and 15 unknowns.

$$\left\{ \begin{array}{lll}
\text{Pressure drop} & \text{Compartment distension} & \text{Flow continuity} \\
p_{car} - p_{art} = R_{art} q_{art} & p_{art} - p_{bra} = \frac{v_{art} - V_{o,art}}{C_{art}} & \frac{dv_{art}}{dt} = q_{art} - q_{arl} \\
p_{art} - p_{cap} = R_{arl} q_{arl} & p_{cap} - p_{bra} = \frac{v_{cap} - V_{o,cap}}{C_{cap}} & \frac{dv_{cap}}{dt} = q_{arl} - q_{vnl} \\
p_{cap} - p_{ven} = R_{vnl} q_{vnl} & p_{ven} - p_{bra} = \frac{v_{ven} - V_{o,ven}}{C_{ven}} & \frac{dv_{ven}}{dt} = q_{ven} + q_{vnl} \\
p_{jug} - p_{ven} = R_{ven} q_{ven} & p_{cra} - p_{bra} = \frac{v_{cra} - V_{o,cra}}{C_{cra}} & \frac{dv_{cra}}{dt} = q_{sas} \\
p_{spi} - p_{cra} = R_{sas} q_{sas} & p_{spi} - P_{out} = \frac{v_{spi} - V_{o,spi}}{C_{spi}} & \frac{dv_{spi}}{dt} = -q_{sas} \\
\\ 
& \text{Monro- Kellie doctrine} & \\
& v_{art} + v_{cap} + v_{ven} + v_{cra} = V_{tot} & 
\end{array} \right.$$

(A.2)

The system of equations associated to the last variation (diagram C in [FIGURE 2.3](#)) was already described and presented in the main body of this report ([EQUATION 2.5](#)).